BIODIVERSITY ASSESSMENT USING SATELLITE IMAGERY IN SAN JOAQUIN EXPERIMENTAL RANGE, CALIFORNIA.

AMA SERWAH BOAKYE
JUNE, 2023

SUPERVISORS:
Dr. Ing. M. Huesca Martinez
Dr. Claudia Paris

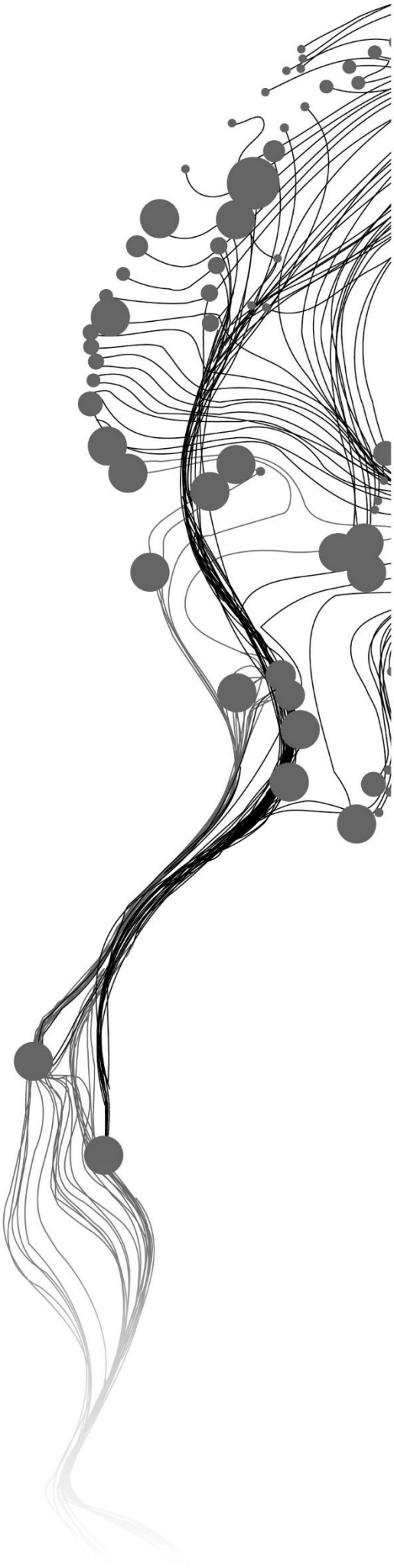

BIODIVERSITY ASSESSMENT IN SAN JOAQUIN EXPERIMENTAL RANGE, CALIFORNIA.

AMA SERWAH BOAKYE
Enschede, The Netherlands, JUNE, 2023

Thesis submitted to the Faculty of Geo-Information Science and Earth Observation of the University of Twente in partial fulfilment of the requirements for the degree of Master of Science in Geo-information Science and Earth Observation.

Specialization: Natural Resource Management

SUPERVISORS:
Dr. Ing. M. Huesca Martinez
Dr. Claudia Paris

THESIS ASSESSMENT BOARD:
Dr.ir. T.A. Groen
Dr. Karine Adelaine

ABSTRACT

In the face of human-induced biodiversity loss, biodiversity monitoring serves as a crucial feedback link supporting the development of informed decisions for conservation management. Remote sensing tool has been demonstrated as a valuable technique for modelling biodiversity across various scales of biological organization, utilizing different levels of spatial granularity and temporal resolution compared to the time and labour-intensive field-based studies for collecting reliable biodiversity data. Hyperspectral data provide extensive information in estimating biodiversity by revealing distinct biochemical and biophysical features of plant species but are limited and expensive. In contrast, multispectral sensors such as Sentinel-2 and Landsat allow monitoring for the continuous acquisition of satellite images at a larger spatial extent with higher temporal coverage. However, their lower spatial and spectral resolution limits their effect in discriminating detailed object characteristics. The Spectral Diversity Hypothesis (SDH) is an emerging approach relying on optical remote sensing to assess and monitor spectral diversity. SDH proposes that the spectral diversity in remote sensing images reflects the spatial heterogeneity within the environment. In this study, the SDH was applied to assess the species richness in the Mediterranean region and investigate the potential of the SDH in biodiversity estimation using multispectral data compared to hyperspectral data.

As such, this study involved pre-processing remote sensing data, reducing data dimensionality using PCA to capture the spectral variation, and applying the K-means classification on selected PCs to identify distinct spectral species in SJER. Next, the data were validated by comparing the field plot data.

The study revealed a weak correlation ($R^2 = 0.0639$ for AVIRIS-NG and $R^2 = 0.0940$ for Landsat 8 data) between spectral diversity and species diversity in the Mediterranean ecosystem, as the application of SDH in this region is characterized by low vegetation cover with strong influence from the soil and non-photosynthetically active vegetation. However, it was revealed that the closed forest areas in the region yielded a better accuracy with R^2 of 0.65 for Landsat, with AVIRIS-NG having an accuracy of R^2 of 0.68. In contrast, the weakest relationships were observed in open forest areas of the region.

Additionally, the study involved spatially and spectrally upscaling the AVIRIS-NG data to simulate Landsat data, aiming to evaluate the impact of the spatial and spectral resolution on species richness derived from remote sensing datasets. The study indicated that the spatial component played a significant role in the discrimination of clusters compared to the spectral component. Reducing the spatial resolution causes the pixels to be more heterogenous as well as to reduce the effect of background information, thereby affecting the spectral mixing of clusters. Consequently, Landsat and AVIRIS-NG images detected consistent patterns of areas with low species richness. Vegetation clusters found in the real Landsat data exhibited spatial consistency with clusters in AVIRIS-NG. Furthermore, The NIR and SWIR spectral domains in both real Landsat and AVIRIS-NG contributed the most to the principal components of AVIRIS-NG and Landsat data.

Overall, these research results contribute valuable insights into analysing remote sensing data for biodiversity assessment for upcoming hyperspectral satellite missions like PRISMA and EnMap for monitoring biodiversity in the Mediterranean region.

Keywords: Mediterranean ecosystem, biodiversity, spectral diversity, species richness, Spectral Variation Hypothesis, Principal Component Analysis, k-means, AVIRIS-NG, Landsat, upscaling.

.

ACKNOWLEDGEMENTS

His word says, "For I can do all things through Christ who strengthens me." And indeed, He has been my strength from the start to the close of this research. Thank you God for guiding me through this academic journey.

To my supervisors, Dr Ing. Margarita Huesca Martinez and Dr Claudia Paris, I extend sincere appreciation for the invaluable guidance, support, and expertise in shaping my thesis research. Your insights, feedback, and encouragement have been instrumental in my academic growth. Further thanks go to Dr Ir. Thomas Groen for providing valuable comments during the proposal and midterm assessment.

To my constant source of motivation, my beloved mother, sisters and father, thank you for your unwavering love and support throughout this endeavour.

To my friends Pearl Adjei-Kumi, Louisa Badger, Sandra Annobil, Sally Sampson, Amanda Wiafe-Akenteng, Joel Nii Nortey Dowuona, Eric Biney, and Albert Ofori, I thank you all for your selfless support and encouragement during my study. Your constant cheering and unwavering belief in my abilities kept me going when things got tough. Your support meant the world to me.

Again, I would also like to express my appreciation to LP Florence Sena Amponsah of Compassion International Ghana for being my biggest support system outside of the Netherlands and advising me during my study.

Finally, I am grateful to Mr Etse Lossou; for all the guidance and support given to me during my study.

TABLE OF CONTENTS

LIST OF FIGURES

APPENDIX

LIST OF TABLES

LIST OF ABBREVIATIONS

APEX	University of Zürich's Airborne Prism Experiment
ARIMA	Autoregressive Integrated Moving Average
AVIRIS-NG	Airborne Visible/Infrared Imaging Spectrometer Next Generation
BFAST	Breaks For Additive Seasonal and Trend
CAO	Carnegie Airborne Observatory (
CZ NETWORK	Critical Zone Network
DBH	Diameter at Breast Height
EBV	Essential Bio
EM	Electromagnetic Spectrum
EnMAP	Environmental Mapping and Analysis Program
EVI	Enhanced Vegetation Index
FAO	Food and Agriculture Organisation
GEE	Google Earth Engine
HISUI	Japanese Hyperspectral Imager Suite
IDL	Interactive Data Language
IISD	The International Institute for Sustainable Development
IUCN	The International Union for Conservation of Nature
JPL	Jet Propulsion Laboratory
LAI	Leaf Area Index
MODIS	Moderate Resolution Imaging Spectroradiometer
NASA	National Aeronautics and Space Administration
NDVI	Normalised Difference Vegetation Index
NEON	National Ecological Observatory Network
NIR	Near-infrared region
NSF	National Science Foundation
PC	Principal Components
PCA	Principal Components Analysis
PRISMA	PRecursore IperSpettrale della Missione Applicativa
RGB	Red Green Blue
SAVI	Soil Adjusted Vegetation Index
SDGs	Sustainable Development Goals
SDH	Spectral Diversity Hyphothesis
SFF	Spectral Feature Fitting
SJER	San Joaquin Experimental Range
SVH	Spectral Variability Hypothesis
SWIR	Short-wave Infrared Region
UN DESA	United Nations Department of Economic and Social Affairs
UNEP	United Nations Environmental Programme
VNIR	Visible Near-infrared
VSWIR	Visible to Shortwave Infrared
WHO	World health Organisation

1. INTRODUCTION

1.1. Background

Biodiversity is defined as the range of living organisms or functional characteristics in an ecosystem or landscape (Cardinale et al., 2012). It provides a variety of functional traits, such as photosynthesis and carbon sequestration that improve productivity and energy fluxes which provide ecosystem services to humans and serve as cushions to climatic events (UNEP, 2018). Through ecosystem services, biodiversity accounts for 50% to 90% of the income generated by the rural poor and supports global and regional food security, particularly for the deprived groups (UNEP, 2018). According to UN DESA (2021). 83% of the poor are in rural areas. These deprived groups in the rural setting live on less than $ 1.90 per day and are socially marginalized and excluded with limited access to basic needs and employment opportunities (Gondwe, 2019). The rural poor depend on the environment for their livelihoods, mainly through agriculture (Gondwe, 2019).

The accelerating global change has grave effects on biodiversity, and this has rippling adverse effects on mankind (Isbell et al., 2017). Human activities have majorly contributed to this global change and have caused rising temperatures, which have affected rainfall patterns and extreme weather events, altering the natural habitats of species. Biodiversity loss affects the efficiency of ecological functioning. These effects of functional characteristics and dependence of species on one another can result in species extinction, affecting life-sustaining ecosystem services provided to humans. In addition, these outcomes of biodiversity loss affect the availability of highly nutritional food, food security, medicines and wood for human use and heighten climate change (Buotte et al., 2020). According to FAO (2019), the farmers' variety of foods is reducing at an unprecedented rate and becoming homogeneous due to biodiversity loss. Moreover, close to 20% of wild species contributing to domestic food availability have also been classified as threatened (IUCN, 2021). Moreover, biodiversity loss also increases the prevalence of pests and infectious diseases as a result of the altered interaction of species (WHO, 2015).

This research will focus on forests, which are habitats for 80% of terrestrial biodiversity (Raft & Oliier, 2011). In particular, forests in the Mediterranean climate regions are home and a hotspot for significant levels of endemic plant species (Cowling et al., 1996). The Mediterranean regions cover the Mediterranean Basin (Cyprus, Malta, Greece, as well as part of Portugal, France, Italy, and Spain); central Chile; southwestern and southern Australia, California and southern Africa. These 5 world Mediterranean regions occupy less than 5 percent of the world's total land areas yet contain 20% of the world's vascular plant species (Cowling et al., 1996). Unfortunately, these highly diversified plant species in the Mediterranean areas are threatened with habitat loss and transformation due to numerous fire outbreaks, intensive agricultural activities and extreme climatic events presenting substantial challenges in plant growth. This can affect the population of these rare species in these Mediterranean areas (Cowling et al., 1996). Plana et al. (2016) highlighted that rampant fire outbreaks occur during dry, hot summer periods because of the climatic and biophysical setting of the Mediterranean regions. These areas could lead to a tremendous proportional change in biodiversity and perhaps face extinction in the future. Since biodiversity is a prominent factor reflected in many SDGs and their related targets (UNEP, 2018), improving biodiversity, and preventing biodiversity loss is vital to achieving the Sustainable Development Goals (SDGs) (IISD, 2019). The UN

(United Nations) common approach to biodiversity has been approved for the integration of nature-based solutions in UN policy formulation and implementation (UNEP, 2021). In addition, averting the societal consequences of biodiversity loss led to reaffirming the Aichi Targets for 2020 by Parties to the UN Convention on Biological Diversity (CBD) (Pereira et al., 2013).

A wide range of studies has been done to estimate forest biodiversity. Alpha, Beta and Gamma diversity are the three most commonly used biodiversity measures (Whittaker, 1972). Alpha diversity relates to local-scale species diversity, where the number of species (species richness) or species abundance in a standard size is measured (Whittaker, 1972). On the other hand, beta diversity highlights the biological evolution of the species and focuses on the difference in the composition of species among communities across space (Whittaker, 1972). Gamma diversity measures the total species diversity in a landscape by finding the product of alpha diversity within the community and the beta diversity amongst the communities (Whittaker, 1972).

Species diversity is renowned for serving as a proxy for biodiversity due to its correlation with genetic diversity and ecosystem functioning (Colwell & Coddington, 1994). According to Chiarucci et al. (2011), although several indices have been developed to estimate species diversity, no standard index has been defined to measure species diversity. Indeed, the current major challenge in estimating biodiversity is the availability of a common global methodology to monitor biodiversity change and provide timely data (Cardinale et al., 2012; Pereira et al., 2012). Chiarucci et al. (2011) assessed the importance of the various species diversity and species evenness matrices from existing literature and recommended indices such as the Shannon diversity index, Pielou's index, and Q-statistics evenness to be used in biodiversity conservation and management. However, according to Chiarucci et al. (2011), the indices (such as the Shannon diversity index, Pielou's index and Q-statistics evenness, and so on) had setbacks in estimating biodiversity since there were limitations in estimating species abundance and species evenness at larger spatial extents. In contrast, Dornelas et al. (2014) argued that there is no change in species diversity but in species composition through time.

Remote sensing technology plays a crucial role in supporting biodiversity monitoring. Indeed, remote sensing data can provide information on a particular area at various spatial extents, with shorter revisit times and lower costs than the classical field survey. Huesca et al. (2015) argued that traditional field surveys are mostly costly and involve a lot of time and financial resources with lower spatial extents examined. The availability of several satellite imaging systems, such as Landsat and Sentinel, provides an unmatched opportunity to monitor species at several time intervals (Zhao et al., 2022). Madonsela et al. (2017) identified the best vegetation index in estimating species diversity by comparing vegetation indices in Landsat 8 multispectral data (NDVI, EVI, SAVI, SRI) with alpha-diversity index (Shannon index, Species richness index and Simpson index), using Principal Component Analysis (PCA). Although the study singled out the best vegetation index computed at very high spatial resolution in detecting vegetation species diversity, the study highlighted that lower spectral resolution results limited the detection of slight changes in the estimation of species.

The last three decades of advancement in imaging spectroscopy have provided some airborne and spaceborne sensors that can be extremely useful for monitoring forest biodiversity. Notable airborne sensors include NASA's Airborne Visible InfraRed Imaging Spectrometer (AVIRIS-NG), Australia's HyMap, Carnegie Airborne Observatory (CAO) and the University of Zürich's Airborne Prism Experiment (APEX) (Rast & Painter, 2019; Cocks et al., 1998). Recent spaceborne hyperspectral sensors, although at medium spatial resolution Precursore IperSpettrale della Missione Applicativa (PRISMA), Environmental Mapping

and Analysis Program (EnMap), Japanese Hyperspectral Imager Suite (HISUI) (Müller et al., 2012; Rast & Painter, 2019). Palmer et al. (2002). presented the Spectral Diversity Hypothesis (SDH), assuming that there is a linear correlation between the species diversity of a sampled area and the spectral diversity of that area. The higher the spectral variability in the image, the higher the heterogeneity in the environment(species diversity). The SDH has been employed in several studies to assess biodiversity. For instance, Heumann et al. (2015) utilized hyperspectral data to evaluate wetlands based on the Spectral Variability Hypothesis. Onyia et al. (2019) investigated the applicability of the Spectral Variability Hypothesis (SVH) in the context of oil pollution impacts on biodiversity using vegetation species as indicators. Féret & Asner (2014) also estimated biodiversity in the Peruvian Amazon using hyperspectral data based on the spectral diversity approach by estimating the Shannon diversity index for alpha diversity and Bray-Curtis dissimilarity for beta diversity. Field data were compared with the spectral diversity of the image derived. It was discovered that there was a challenge in identifying which specific spectral domain in the Principal Components (PC) contributes the most to the estimation of biodiversity based on the specific physical and chemical components.

Even though hyperspectral spectral reflectance data offer an extensive variety of information in estimating biodiversity by revealing distinct biochemical and biophysical features of plant species (Anand et al., 2022), hyperspectral data acquisition is more expensive and has a lower spatial and temporal coverage than multispectral data. On the other hand, freely obtainable datasets from multispectral sensors such as Sentinel-2, Landsat, and MODIS allow for the continuous acquisition of satellite images but have limited use in providing detailed spatial and spectral information in discriminating species. Therefore, it is imperative to study differentiating spectral information on species diversity with greater spatial extents and temporal frequency, which can be open access and inexpensive at a lower spatial resolution. This study expanded on the research conducted by Féret & Asner (2014) by applying the Spectral Diversity Hypothesis (SDH) in the Mediterranean region instead of the tropical forest and using multispectral data instead of hyperspectral data as employed in their research. Additionally, this study examined the applicability of SDH to satellite multispectral data and future hyperspectral data with lower spatial resolution for Mediterranean ecosystems. The overarching goal of this study was aimed at estimating species richness in Mediterranean ecosystems using multispectral (Landsat) data.

1.2. Problem Statement

This study was conducted in the San Joaquin Mediterranean region, the most lucrative agricultural region in the United States of America (Fernandez-Bou et al., 2022). Unfortunately, due to water scarcity in San Joaquin, most current agricultural practices compete with ecosystems for water access. Further, these intensive agricultural footprints and urban developments result in habitat loss and the establishment of invasive species (Fernandez-Bou et al., 2022). As a result, the ecosystem of the San Joaquin Valley is one of the most degraded in California(Fernandez-Bou et al., 2022).

Plants typically in the Mediterranean region are known to adapt to hot, dry summers with low moisture. California is described with extensive blue oak woodlands with the lower foothills of the Central Valley predominated by savannas, spanning about 12,000 km^2 (Huesca et al., 2021). The blue oak (*Quercus douglasii*) is California's most dominant and xeric-tolerant endemic oak species. Sadly, California suffered severe effects from the worst drought in the millennia between 2010 to 2016 (Huesca et al., 2021). Fettig et al. (2019) also noted that 2014 and 2015 were the warmest years in California's records. The blue oak species were heavily affected by tree mortality primarily due to the rate of high temperature and low rainfall conditions from 2013-2015, with an average mortality of 10% over the San Joaquin Experimental Range (SJER) during the drought (Huesca et al., 2021). Furthermore, although the drought began in 2013, the

mortality rate became noticeable from the year 2014 to 2015 with a reduction in canopies sizes, water content and LAI (Huesca et al., 2021). This cause of tree mortality was not due to over-grazing because these plants would have to be seedlings for them to be affected. Besides, the high temperature incidences are predicted to be more frequent by mid-century (Ullrich et al., 2018).

Notwithstanding, logistic and financial constraints limit field observations of species not only in space but in time. This renders the overview of evidence from species at various geographic and climatic zones challenging (Dronova & Taddeo, 2022). In addition, the high cost of data acquisition of hyperspectral data makes it unfeasible to monitor biodiversity at a larger spatial extent with higher temporal coverage. Although Spaceborne hyperspectral systems such as PRISMA and ENMAP have been launched, they do not have a wider temporal component for monitoring biodiversity at a higher temporal resolution (Foerster et al., 2016; Loizzo et al., 2019). Upcoming hyperspectral satellite missions like PRISMA can apply this research approach as a benchmark for monitoring biodiversity at a wider time series and lower spatial resolution.

Several research works on biodiversity monitoring (Anand et al., 2022; Féret & Asner, 2014) have been based solely on tropical forest areas, while the Mediterranean areas have not been extensively explored. Against the background, this research applied the SDH approach to assess the species richness and investigate the potential of the SDH approach in biodiversity estimation using multispectral data compared to hyperspectral data in the Mediterranean forest. With multispectral data proven to measure biodiversity, further studies can delve into the temporal behaviour of the species, including adaptation strategies used by species in the Mediterranean ecosystem. Again, this novel study will help provide affordable, detailed spectral information on biodiversity at a larger spatial scale in the Mediterranean regions using Landsat data. This is a vital attempt to minimize biodiversity loss by identifying priority areas of biodiversity loss. The information acquired on biodiversity assessments in the area will also support policy making to ensure biodiversity conservation in the Mediterranean region, water balance, and even carbon sequestration to combat climate change.

1.3. Objectives

The main objective is to assess the species richness in the Mediterranean ecosystem using multispectral data. Furthermore, this study intends to demonstrate that the spectral features (SDH) identified can still measure species richness even when their signals are weak to detect at lower spatial and spectral resolutions leading to its application across time.

1.3.1. Sub-specific Objectives

- Estimate species richness using hyperspectral data based on the SDH approach in a Mediterranean ecosystem.
- Understand the variation in species richness when applying the SDH approach to optical data characterized by different spatial and spectral resolutions.

1.4. Research Questions and Hypothesis

To execute the main objective and sub-specific objectives outlined, the research questions and corresponding hypothesis are:

1) How do estimates of spectral diversity with 4m hyperspectral data relate to species richness in the Mediterranean ecosystem?

H_1: There is a relationship between spectral diversity with 4m hyperspectral data and species richness in the Mediterranean ecosystem.

2. a) How do estimates of spectral diversity with simulated Landsat data (30m) relate to species richness in the Mediterranean ecosystem?
H_1: The spectral diversity with simulated Landsat data (30m) has a relationship with the species richness in the Mediterranean ecosystem.

2. b) How do estimates of spectral diversity with Upscaled hyperspectral data (30m) relate to species richness estimations in the Mediterranean ecosystem?
H_1: Upscaled hyperspectral data (30m) has a relationship with the spectral diversity in the Mediterranean ecosystem.

2.d) How do the spectral diversity with Landsat data (30m) relate to species richness estimations in the Mediterranean ecosystem?
H_1: The spectral diversity with Landsat data (30m) has a relationship with the species richness estimations in the Mediterranean ecosystem?

2. STUDY AREA AND MATERIALS

2.1. San Joaquin Experimental Range (SJER)

The San Joaquin Experimental Range (SJER) extends an area of 1806ha and is situated in the southern Sierra Nevada foothills in Madera County at approximately 37°05'N 119°43'W (Figure 1). This study region has been involved in livestock grazing since its inception in 1934. SJER, California's first research station, has contributed knowledge on patterns and processes in the Mediterranean ecosystem for educational and research purposes (Purcell et al., 2007). SJER has been authorized to be a core site of the Southwest Pacific area. In addition, the SJER is part of the National Ecological Observatory Network (NEON) terrestrial site; the NEON site is part National Science Foundation's (NSF) initiative and is also associated with the southern Sierra Critical Zone Observatory (CZ Network, 2020).

With an average annual temperature of 16.6°C and average precipitation of 513 mm/yr. (CZ Network, 2020), it has been observed that there has been an increase in average maximum temperatures by 1°F (0.6°C) from 1950 to 2020 every year (Fernandez-Bou et al., 2022). The air (mean monthly) temperature typically ranges between 4°C to 10°C in the cool, wet winter season and 24°C to 27°C in the hot, dry summer period, with daily temperature peaks easily exceeding 38°C. The rainfall season usually occurs from October or November to April or May.

The vegetation species in SJER are diverse, with blue oak (*Quercus douglasii*) woodland being the predominant type. Other notable species include Mariposa manzanita (*Arctostaphylos viscida mariposa*), hoary coffeeberry (*Rhamnus tomentella cispidata*), interior live oak (*Quercus wislizenii*), chaparral whitethorn (*Ceanothus leucodermis*), wedge leaf ceanothus (*Ceanothus cuneatus*), grey pines (*Pinus Sabiniana*), and more. Among the vegetation species, the grey pine and the interior live oak are evergreen species, whereas the blue oak species is deciduous, starting greenness in April and ending in November (Miraglio et al., 2022). Areas in SJER have the overstory predominantly composed of blue oak, with shrubs and herbaceous species dominating the understory. Blue oak is known for its preference for the lowest and driest elevation zone, situated above the central valley floor of California. It thrives on the western foothill slopes of the Sierra Nevada Mountains. The blue oak is renowned for its exceptional longevity. Most Blue oak trees have tree ring ages that commonly span 500 years, while a few exceptional individuals have demonstrated ages of up to 600 or potentially even 700 years (Stahle et al., 2013). Grasses occur in abundance across all vegetation structures, forming a mosaic across gently sloped terrain where the overstory is lacking (Miraglio et al., 2022). The region's shrubs (interior live oaks) are typically sparsely populated (Newman & Duncan, 1973).

The soil types, specifically Ahwahnee and Visalia series, originate from granite and have a limited capacity to retain water (Newman & Duncan, 1973). The SJER area does not host permanent streams but is abundant in intermittent streams, swales, and springs. During the winter months, small drainages usually carry surface flow. The watershed of SJER ultimately drains into Cottonwood Creek, which serves as a tributary of the San Joaquin River.

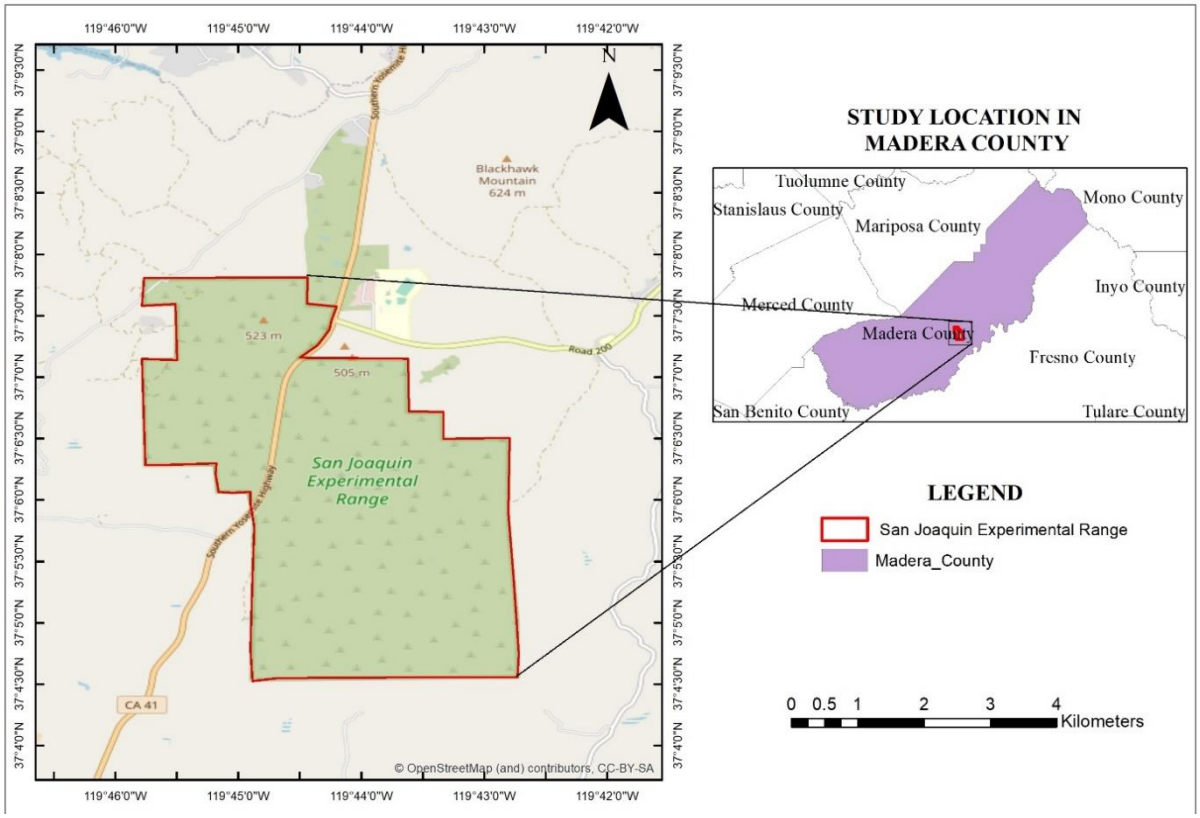

Figure 1. Considered study area located in the San Joaquin Experimental Range, Madera County, California.

2.2. Remote Sensing Data

2.2.1. Hyperspectral Data

This research exploited the hyperspectral data acquired with the Airborne Visible/Infrared Imaging Spectrometer Next Generation (AVIRIS-NG) sensor mounted aboard the NASA ER-2 aircraft platform. The data acquisition was carried out by the Jet Propulsion Laboratory (JPL) during the airborne summer campaign in 2014 for the Hyperspectral Infrared Imager (HyspIRI mission) over SJER. The hyperspectral sensor AVIRIS-NG was designed to take over from AVIRIS-classic with better radiometric and spatial performance.

Known as the latest and most advanced hyperspectral sensor, AVIRIS-NG has 432 spectral bands ranging from 346.3nm–2505nm spectral range (Aljunid & Manjaiah, 2021) and a high signal-to-noise ratio. Its high spatial resolution (4m) and spectral resolution, along with more than 95% Instantaneous Field of View (IFOV), have facilitated the identification and mapping of spectral signatures in several applications, including the prediction of foliar nutrients, species discrimination and carbon stock (Thompson et al., 2015; Zhang et al., 2021).

The AVIRIS-NG data was downloaded from the NASA JPL website. This hyperspectral imagery was captured on June 11th, 2014, at 20:46 hrs PST. Fifty-nine bands from the AVIRIS-NG image were excluded by NASA JPL due to their occurrence in water absorption, specifically column water vapour, liquid absorption, and ice absorption, with 373 retained bands. These bad bands were found in the wavelengths 346.3 nm to 376nm, 1348nm to 1428.2nm and 1778.8nm to 1949nm. Also, NASA JPL performed radiometric calibration and georeferencing processes on the AVIRIS-NG image using a methodology

developed by Thompson et al. (2015) and atmospheric correction on the AVIRIS-NG using the approach described by Gao et al. (1993) to retrieve the surface reflectance values from the AVIRIS-NG data. A specific aircraft strip line image was selected since the NASA JPL flight lines provided did not cover the entire study area to ensure comprehensive coverage. This selected image maximized the number of field plots sampled within the SJER area.

2.2.2. Multispectral Data

The study also utilized Landsat data due to its unrestricted availability and continuous earth observation data spanning the past 40 years (Banskota et al., 2014). As a long-running space-based earth imagery system, Landsat has been used for several research applications (Boori et al., 2021; Kefalas et al., 2018; Michela et al., 2022; Sousa & Small, 2018).

In particular, the Landsat-8 Operational Land Imager (Landsat-8 OLI) sensor was used for this study. To ensure temporal coherence and facilitate meaningful comparisons and analysis with the selected AVIRIS-NG data, the Landsat-8 satellite image acquired on June 8th, 2014, was considered. The data were downloaded from the Google Earth Engine (GEE) platform. The Level 2 Landsat 8 data comprises 7 spectral bands across the visible to the shortwave infrared region (VSWIR) of the electromagnetic (EM) spectrum.

Landsat-8 has a spatial resolution of 30m and revisits a specific location approximately every 16 days, resulting in 22 to 23 images a year (Zhu, 2017). Pervez et al. (2016) reported that Landsat-8, due to its 12-bit data quantization, improves the signal-to-noise radiometric performance of the sensor. This enhancement has significantly increased the effectiveness of Landsat-8 for landcover mapping and species diversity purposes (Madonsela et al., 2017).

2.3. Field Data

This study used secondary field data collected as part of the NASA Hyperspectral Infrared Imager (HyspIRI) Mission's Airborne Campaigns from the summer of 2013 and 2014. The field data collection focused on tree species within the region, which was primarily used to validate species richness estimations in this study.

The field survey utilized the stratified random sampling method to capture variability in species composition and canopy cover across SJER. The data collection was conducted in 60 by 60m plots, which were sufficiently homogenous to represent 1ha plots. Within each 60 by 60m radius plot, a radius of 20m subplots was established. A total of 542 tree inventory data were collected at the SJER from the years 2013 to 2015. The stratified random sampling approach used was to ensure efficiency in field estimations within every subplot aligning the AVIRIS-NG data. The field campaign was repeated in several seasons, with emphasis placed on sampling plots dominated by deciduous, annual, or perennial trees to depict their temporal evolution over the years. This plot level inventory included the geolocation of the various tree species, canopy base height, diameter at breast height (DBH), canopy width, and a description of the state of health on the trees. During its pre-processing, field plots located outside the selected aircraft strip line region were identified and excluded. Field plots with missing relevant information, such as plot names, were also removed. As a result, 399 sample points remained, which were already grouped at the plot level, resulting in a total of 40 plots.

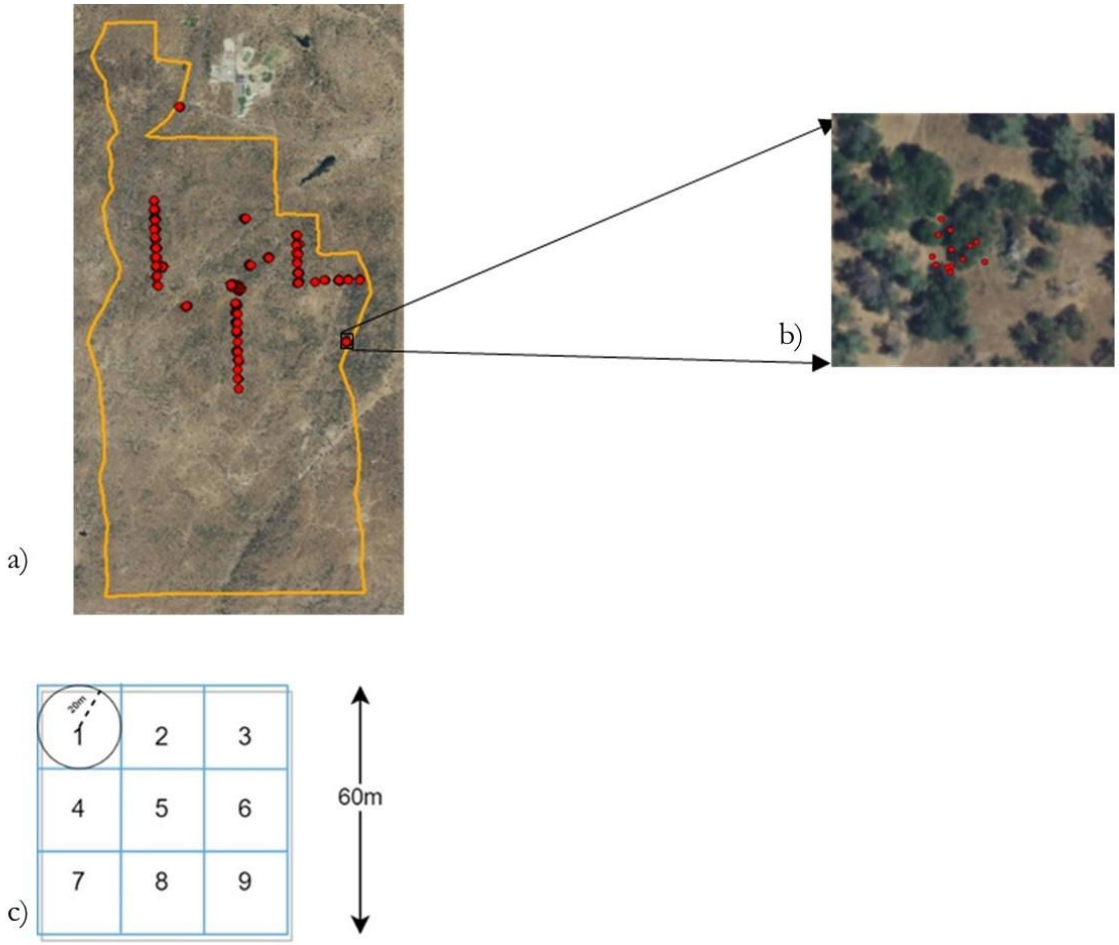

Figure 2 Example of: a) One Strip Line Aerial View acquired over the SJER, b) Field Plots Sampled highlighted in red, C) 20m Radial Subplots Within 60 x 60m Plot.

3. METHODOLOGY

3.1. Research Methodology

This chapter, divided into two sections, details the operational steps adopted in this study. The first section focuses on biodiversity estimation when using AVIRIS-NG and Landsat 8 data, while the second section explores the impact of upscaling the spatial and spectral resolutions of the original hyperspectral data on biodiversity estimation. The procedures involved in the 2 phases are detailed in the sub-sections below. Figure 3 depicts the flowchart of the methodology utilised in this study.

.

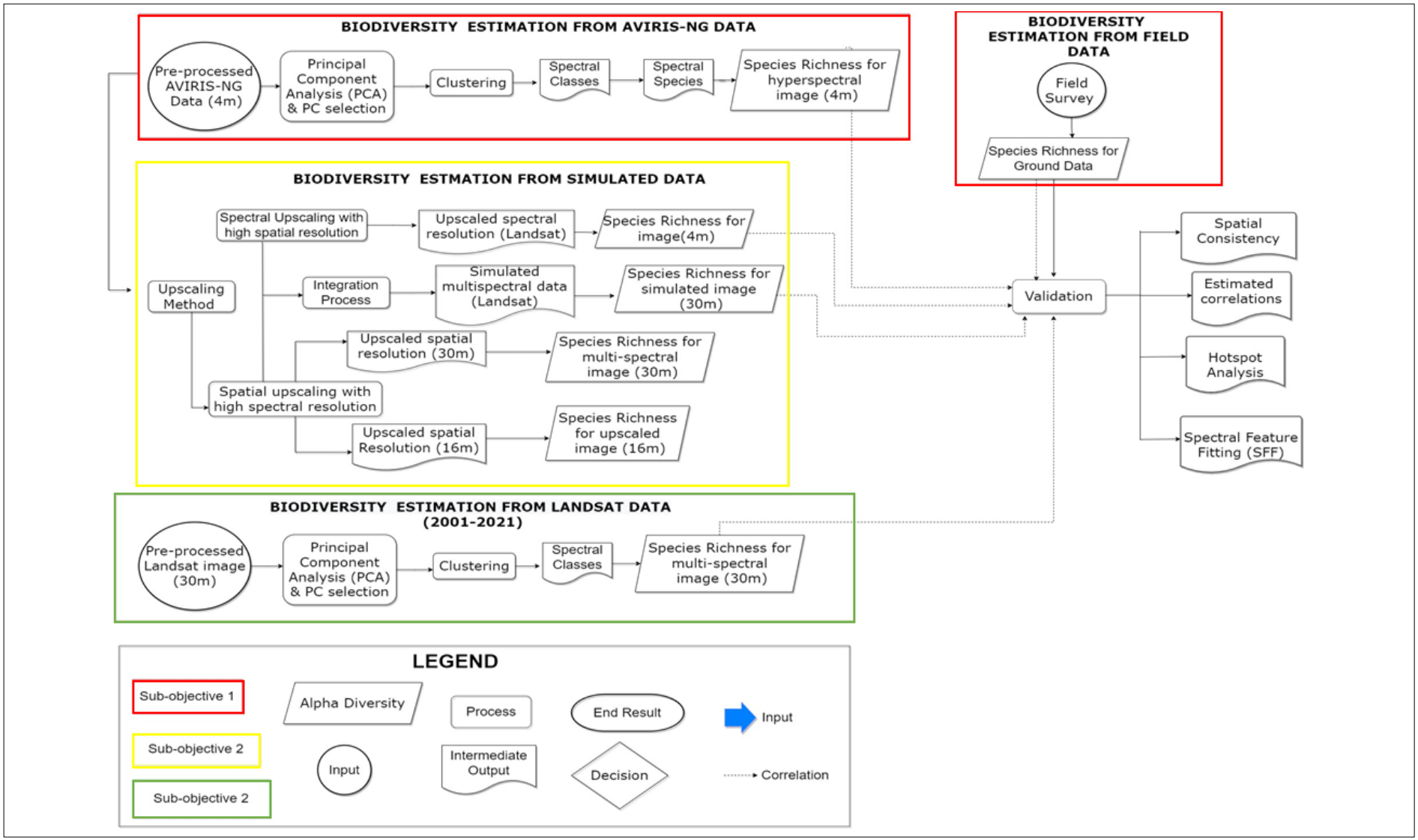

Figure 3 Study Methodology Flowchart

3.2. Pre-processing

Prior to carrying out the biodiversity estimations and performing the upscaling procedure., pre-processing steps were executed. The pre-processing involved three main steps: 1) the identification and masking out of non-vegetative pixels, 2) outlier identification, and 3) the normalization of images per band.

The Landsat data and the high spatial resolution QGIS Base Map available in QGIS were used to identify the non-vegetative pixels. First, the NDVI is estimated considering the Landsat data for the whole study area. Then, the pixels with NDVI less than 0.3 were visually inspected using the very high-resolution QGIS Base Map images to determine which pixels must be discarded. Most importantly, the areas masked out in the Landsat data were also excluded in the AVIRIS-NG data to generate consistent results.

Moreover, the outlier identification (Heymann et al., 2012) and the data normalization (Singh & Singh, 2022) steps were executed on each remote sensing image per band. Linear scaling was performed to adjust the spectral values into a Gaussian distribution. The outliers were automatically identified per band using high (95^{th} percentile) and low quantile (5^{th} percentile) thresholds. In the case of values identified to exceed the high quartile threshold, the high threshold value was substituted. On the other hand, values detected below the low quartile threshold were substituted for the low threshold value. The bands were then normalized by subtracting the minimum value from each band and dividing it by its range using Equation 1 below. The normalized values are assigned back to the respective pixels in the image. This step allows for the comparison of the various images and the removal of noise.

$$img = (band - min(band)) ./ (max(band) - min(band)) \quad \text{(Equation 1)}$$

; where img represents all bands in the image matrix.

3.3. Biodiversity Estimation based on SDH

The estimation of alpha diversity using the SDH approach encompasses steps illustrated in Figure 4.

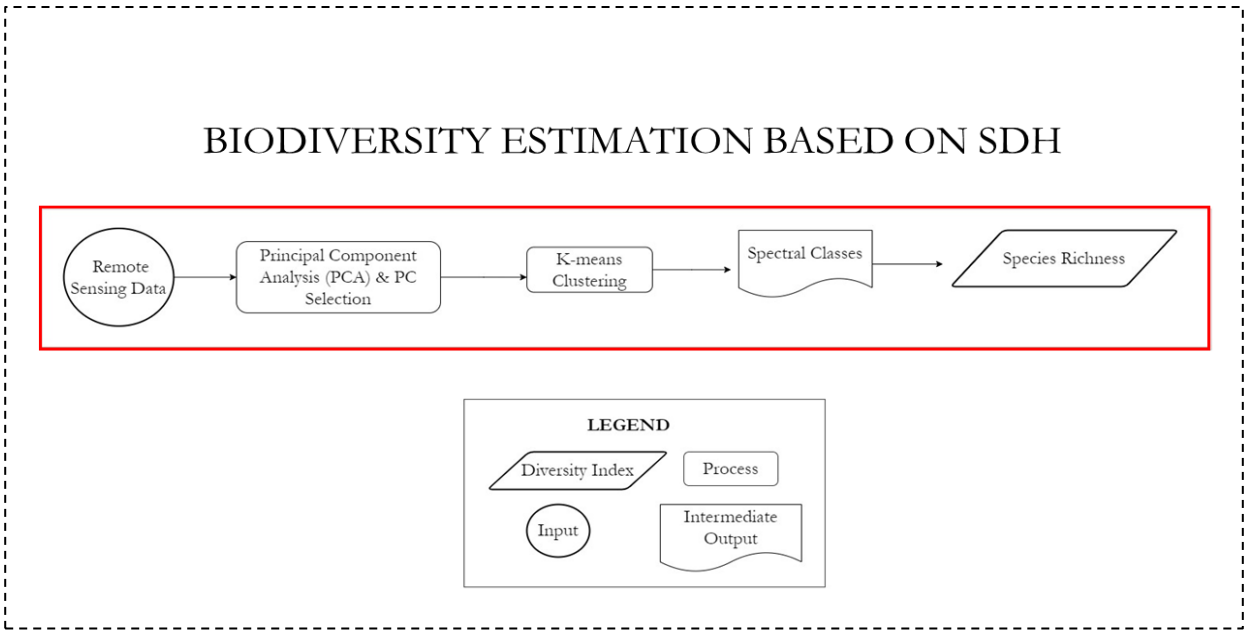

Figure 4 Biodiversity Estimation using the SDH Approach

First, the Principal Component Analysis (PCA) was used to reduce the dimensionality of the pre-processed remote sensing images. Then, an unsupervised clustering algorithm was applied considering the reduced feature space made up of the selected Principal Components (PCs). The clustering result is used to derive spectral classes or species, using the Davies Bouldin index to determine the optimal number of classes. The spectral species maps were transformed into species richness estimations at 1 ha spatial resolution.

3.3.1. Principal Component Analysis (PCA)

PCA was performed on the pre-processed images. Singh (1993) describes PCA as a multivariate statistical technique employed in the field of remote sensing to reduce the dimensionality of image data and image encoding. This aims to extract the maximum amount of information from the original bands to the least number of PCs (Estornell et al., 2013). This orthogonal transformation involves converting a set of correlated variables (original image bands) into uncorrelated variables (PCs), which support the removal of redundant bands in the spectral range to select relevant principal for better performance and higher accuracy. The PCA was performed using the ENVI classic software (v. 5.6.3). The PCs were visually explored and selected based on the eigenvalues and cumulative percentage of variation explained in the original data. The visual exploration of PCs aimed to assist in revealing the pattern of species richness in SJER. The first principal component (PC) band contains most of the information, followed by the subsequent principal components. The second PC band captures the second-largest source of variability orthogonal to the first PC band, and the third PC band captures the third-largest source of variability orthogonal to the first two PC bands.

3.3.2. Maximum number of Spectral Species Estimation

The spectral classes (called spectral species in this research) were determined by applying an unsupervised k-means clustering algorithm to the selected PC bands of the different remote sensing images (real and simulated data) considered in this study. First, a subset of pixels are randomly selected for classification based on similarity. Subsequently, after several iterations, a pre-defined number of spectral classes based on the homogeneity within those classes was defined. ENVI classic software (v.5.6.3) was used to carry out the k-means clustering for spectral species classification.

During the k-mean clustering, each vegetated pixel is assigned to a spectral class based on the shortest Euclidean distance between the pre-specified centroids and the spectral values recorded for the pixel. Hence, the spectral classes have a relationship with the species diversity.

The number of clusters chosen for unsupervised image classification, such as k-means, can impact both the spatial and spectral information of the resulting segmented image (El Abbassi et al., 2021). Considering different remote sensing data, the Davies Bouldin index was employed to determine the optimal maximum number of classes that can be discriminated in the study area. This cluster separation measure is based on the ratio of compactness within clusters to separability between clusters (Davies & Bouldin, 1979). The separability of the cluster is calculated by computing the minimum distance between each point in a cluster and the centroids of other clusters. The compactness is measured by estimating the average distance between each point in a cluster and its centroid. This elbow method (Davies Bouldin Index) relies on the concept of diminishing returns in variance explanation as more clusters are included. A lower Davis Bouldin Index is associated with better clustering performance (Davies & Bouldin, 1979). MATLAB software was used to estimate the Davies Bouldin Index. At the end of this step, the corresponding spectral species map for each considered remote sensing data is developed.

3.3.3. Species Richness

The most commonly used alpha diversity metric, species richness, was calculated by counting the number of unique species in a 1-ha moving window. Chao & Chiu (2016) define species richness as the number of

unique species present in a particular area or ecosystem. This index was calculated using a 1-hectare moving window, with the number of pixels adjusted to fit the varying spatial resolution of the generated spectral species maps (spanning from 4m to 30m). Thus, the resulting mapping units, the output of the species richness estimations, have a 1ha spatial resolution.

The species richness calculations for the remote sensing images were done using the ENVI IDL v.8.2.0 (Interactive Data Language) programming language. The number of spectral class maps are transformed into image bands, with each representing a respective spectral class. Typically, species richness provides information on the species' presence-absence information for a locality. Pixels with more than 0 bits per band are given a value of 1 for presence, whereas pixels with no data are assigned a value of 0 for absence. These binary values were summed across the bands to calculate the number of different species present within a 1-ha window.

The quantification of species diversity primarily emphasized species richness as an alpha diversity metric due to its simplicity and straightforwardness in contrast to more complex metrics such as the Shannon index.

3.4. Biodiversity Estimation for Simulated Data

The second sub-objective of the study aims to study the impact of the spatial and spectral resolutions on biodiversity estimation using the SDH approach, which is visually represented in Figure 5.

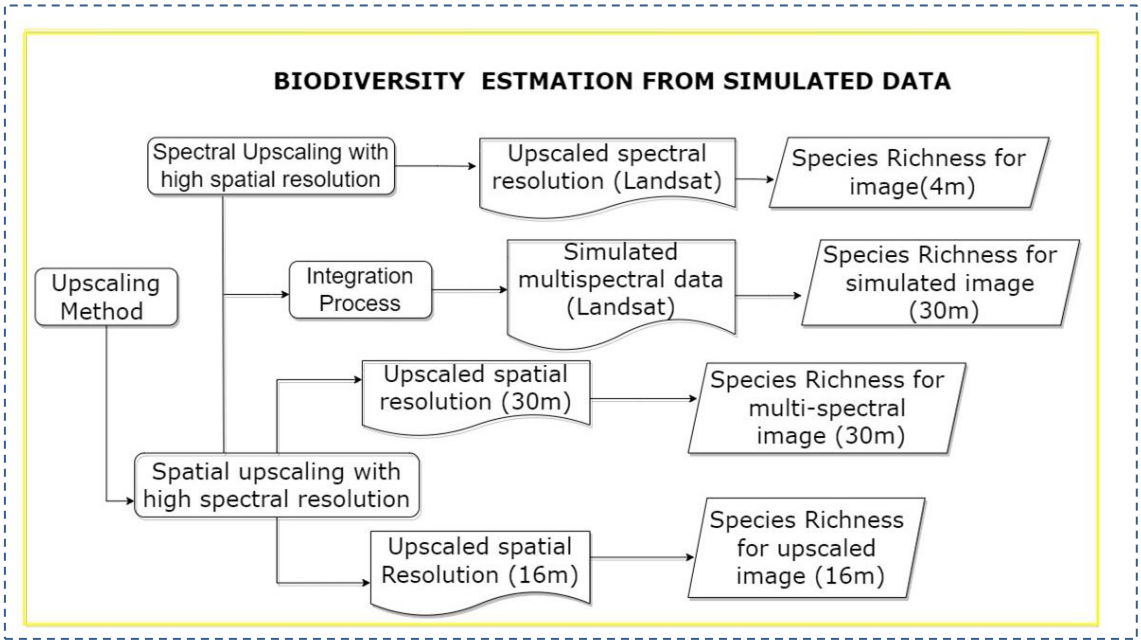

Figure 5 Biodiversity Estimation for Simulated Data

Starting from the AVIRIS-NG hyperspectral data, simulated data were generated by computing spatial upscaling, spectral upscaling and a combination of both in order to generate the simulated version of Landsat data. The upscaling method involves reducing the finer resolution (spatial or spectral) of the image to a coarser representation by combining smaller units to larger units (Markham et al., 2023). At the end of this step, four simulations were generated. These include a spectrally upscaled 4m image (7 bands), a 16m hyperspectral data having spectral properties of the AVIRIS-NG sensor, a 30m hyperspectral data having the spectral properties of the AVIRIS-NG sensor, and a simulated Landsat-8 data.

3.4.1. Spatial Upscaling

In landscape ecology, the spatial resolution (grain) of the considered optical images plays a vital role in mapping biodiversity. When performing the spatial upscaling, the spectral resolutions of the pre-processed AVIRIS-NG data were maintained (373 bands). The AVIRIS-NG spatial resolution (4m) was upscaled to the spatial resolution of an intermediate pixel size of 16m and the multispectral Landsat data spatial resolution (30m). This was executed through the decimation into the two spatial resolutions by resizing the original image with the scale factor of 1/4 (16m) and 1/7 (30m) of its original size each. The blurred images were then downsampled in all directions with a spatial reference similar to the original image. The AVIRIS-NG was subsampled to a 16m spatial resolution to investigate the variation in the alpha diversity index for the 16m resolution data with the AVIRIS-NG before comparing it with the 30m spatially upscaled hyperspectral data. The obtained simulated images had the same spatial extent and georeferencing as the original AVIRIS-NG image.

Spatially upscaled images were used to estimate species richness using all steps outlined in subsection 3.3.

3.4.2. Spectral Upscaling

The spectral upscaling was executed by downgrading the spectral resolution of the pre-processed AVIRIS-NG to the spectral resolution of Landsat 8, maintaining the spatial resolution of the original image (4m). The narrow 373 bands were fused to form broader bands to match the desired Landsat spectral resolution by calculating the spectral responses of the Landsat 8 bands with AVIRIS-NG spectral information. This is based on the band number, central wavelength, and bandwidth (nm) of the Landsat-8 spectral properties.

The biodiversity estimation of the spectrally upscaled image followed the systematic procedure outlined in subsection 3.3.

3.4.3. Simulated Landsat

The simulated Landsat (30m) data were produced by combining both methods outlined in the spatially and spectrally upscaling procedure. The biodiversity estimation described in subsection 3.3 were applied to estimate the species richness of the developed image to untangle the effects of spatial and spectral resolution differences on biodiversity estimations.

3.5. Validation

Validation was done by evaluating the relationship by comparing the species richness estimated when using the field data with the ones obtained with the considered remote sensing images. Moreover, the spatial consistency of the spectral species maps generated using different remote sensing data was evaluated. Finally, the spectral meaning of the clusters obtained was compared with the JPL AVIRIS vegetation spectral library using Spectral Feature Fitting (SFF). Together, these evaluation measures were employed to determine the impact of spatial and spectral variations in biodiversity estimation between the original hyperspectral data, Landsat-8 image and the simulated data.

3.5.1. Biodiversity Estimation of Field Data Species Richness

The species richness was computed for each field data plot by estimating the number of unique species. The study utilized the R package "vegan" v. 2.6-4 for species richness computations.

The study adopted an inductive approach to examine the relationship between the species richness obtained from the field data and the corresponding species richness derived from the different remote sensing

datasets (i.e. AVIRIS-NG, the 4m spectrally upscaled data, 16m hyperspectral data, 30m hyperspectral data, simulated Landsat-8 and Landsat-8). The field points were used to extract the estimated biodiversity indices at various locations on the associated remote sensing images to establish this relationship. This was evaluated using the Pearson correlation test (R^2) to determine the intensity of the relationship between the species richness derived, as seen in Figure 3.

3.5.2. Closed and Open Forest

The study proceeded to investigate the correlation between the biodiversity indices derived from the remote sensing images and field data, explicitly focusing on field points located in close and open forests separately. A two-step process was employed to categorize a sampled field plot as an open or closed forest. First, a visual exploration was conducted using a high spatial resolution to identify points located in a close or open forest. These identified open and closed forests were evaluated based on tree density Gauquelin et al. (2018) mentioned in distinguishing Mediterranean forests. According to the criterion, areas with a tree density of less than 4 individual trees per 1 ha were categorized as open forests. In contrast, areas with a tree crown density exceeding 4trees per 1 ha were classified as closed forests. This lower limit of the closed forest was set at 4 trees by visually examining all sampled plots in the region. The categorisation of the field plots resulted in 70% being in the open forest, while 30% were in the closed forests.

a)

b)

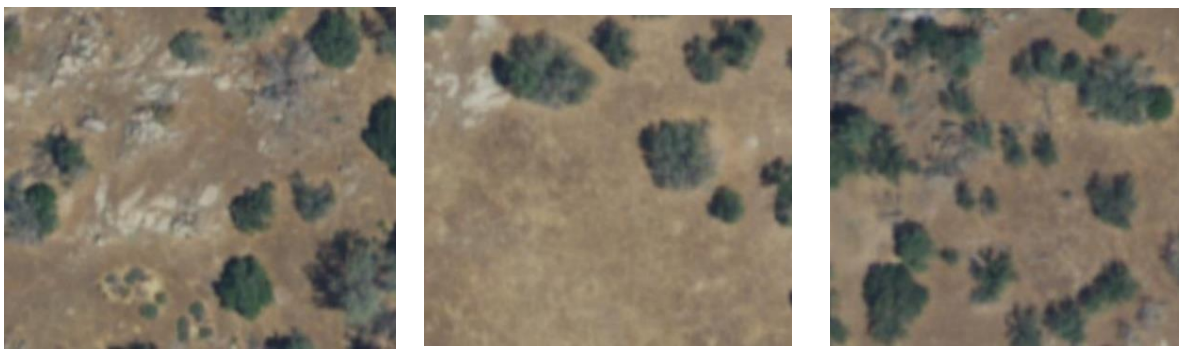

Figure 6 Example of: a) Closed Forest Areas in SJER, and b) Open Forest Areas in SJER.

3.5.3. Spatial Consistency

For better discrimination of clusters in the images, the spatial consistency of the resulting clusters for the various images was evaluated with the spectral species map generated with AVIRIS-NG. Specifically, spatially consistent clusters were identified by examining the similarity of the cluster of the pixels. The number of similar pixels in each image was quantified to evaluate the similarity of pixels within each cluster across the images with the AVIRIS-NG image. Furthermore, the spectral signature of the selected corresponding clusters was verified for similarity using visual examination. Additionally, the images of the spatially consistent clusters were examined on very high-resolution satellite images (QGIS base map) to identify what the clusters represent.

3.5.4. Spectral Feature Fitting (SFF)

Spectral Feature Fitting was conducted to analyze the physical meaning of the clustering results obtained with the aim of associating each cluster with a specific class. SFF is a technique that entails comparing the (unknown) spectra in an image with reference (known) spectra from a spectral library (Roger et al. 1993). The method uses a least-squares fit to determine the similarity.

Regarding the SFF analysis, the JPL AVIRIS spectral library for vegetation was utilized within the ENVI classic software. By comparing the unknown pixel spectra with the reference spectra, the SFF values were calculated. A lower SFF value indicates a higher similarity between the endmember and the average spectra of the cluster (pure vegetation cluster).

The SFF analysis was primarily conducted on the clusters derived from AVIRIS-NG. This comprehensive approach allows for a better understanding of the spectral meaning of the obtained clusters.

3.6. Spatial Pattern Analysis

In the study, a spatial pattern analysis was conducted to identify areas of high and low biodiversity utilizing the Getis-Ord Gi* statistical analysis tool, which serves as an indicator for priority intervention. This tool identifies a significant spatial cluster of pixels with either high (hotspots) or low (coldspots) values (Boori et al., 2021). The z-scores and p-values derived serve as measures of statistical significance and aid in determining whether to reject the null hypothesis or accept it. The null hypothesis assumes Complete Spatial Randomness (CSR) of the pixels or their associated values.

A statistically significant hotspot can be established by a high value pixel having similarly high value pixels surrounding it. Moreover, intensified clustering of high pixel values reflects higher z-scores. Conversely, heightened clustering of low values indicates coldspots, signalled by lower z-scores (Silveira et al., 2021). A high $\pm z$ score with a small p-value indicates clustering of both high and low values. The application of the Getis-Ord Gi* statistic in identifying low biodiversity areas was adopted from a study conducted by Silveira et al. (2021) in estimating areas of biodiversity concern in a spatiotemporal analysis. This assessment of areas with high and low biodiversity was solely based on species richness.

4. RESULTS

This section presents the results obtained through species richness estimations using both real (i.e., AVIRIS-NG and Landsat) and simulated data and reflects on the findings derived from the analysis. Consequently, the chapter examines various aspects, including Principal Component Analysis (PCA), spatial consistency and Spectral Feature Fitting.

4.1. PCA Analysis

This subsection details the results of the selected principal components from the PCA analysis of AVIRIS-NG, spectrally upscaled 4m image, spatially upscaled 16m image, spatially upscaled 30m image, simulated Landsat, and Landsat 8 data. The PC selection for each remote sensing data was based on the eigenvalues resulting from the PCA and the PCs accounting for at least 98% of the cumulative variance in the images (Figure 7). Moreover, the remaining PCs produced only 2% or less of the total (eigenvalue) of the data, as their images appeared to be noise. Table 1. summarises the eigenvalues of the first three PCs for each remote sensing image.

Table 1 PC Bands with Various Eigenvalues and Percentage Variances

Remote Sensing Data	PC Band	Eigenvalue	Percentage Variance
AVIRIS-NG	Band 1	7.352837	89.8
	Band 2	0.555378	6.8
	Band 3	0.163083	2
Spectrally Upscaled 4m Image	Band 1	0.164344	90
	Band 2	0.012020	6.6
	Band 3	0.004275	2.3
Spatially Upscaled 16m Image	Band 1	4.746150	89.8
	Band 2	0.381812	7.2
	Band 3	0.094383	1.8
Spatially Upscaled 30m Image	Band 1	3.963779	89.8
	Band 2	0.325333	7.4
	Band 3	0.074057	1.7
Simulated Landsat Image	Band 1	0.070639	91.3
	Band 2	0.004284	5.5
	Band 3	0.001808	2.3
Landsat 8	Band 1	0.015586	92.2
	Band 2	0.000748	4.4
	Band 3	0.000324	2%

Table 1 shows that the first three PCs contain a significant part of the information. The first three PCs explained 89.8%, 6.8%, and 2% of the variance in the AVIRIS-NG image. In the simulated Landsat image,

the first 3 PCs explained 91.3%, 5.5%, and 2.3% variance in the image. On the other hand, the first 3 PCs of Landsat 8 explained 92.2%,4.4%, and 2% of the total variance in the dataset. The correlation matrix shows that PC1 has a large positive correlation with bands within the red and near-infrared region (701 to 852 nm) for AVIRIS-NG, contributing the most to species variation. PC2 and PC3 are also related to NIR and SWIR bands (1313.2 nm to 2190 nm) and (862.2 nm to 1758.8 nm), respectively.

Similarly, in the case of the simulated Landsat and Landsat, the first three PCs were influenced the most by the bands in the NIR and SWIR range (Table 5 and Table 6). This can be attributed to the high reflectance of vegetation signals in the NIR and its spectral response to dry vegetation in the SWIR.

Moreover, by loading the first three PC images in RGB, as seen in Figure 7, the lower spatially resolution images (spatially upscaled 16m, spatially upscaled 30, simulated Landsat and Landsat 8) captured general and similar dominant pattern as the AVIRIS-NG image although less detailed. Meanwhile, the higher spatial resolution images (the spectrally upscaled 4m image and AVIRIS-NG) captured the spatial grain and intricate pattern.

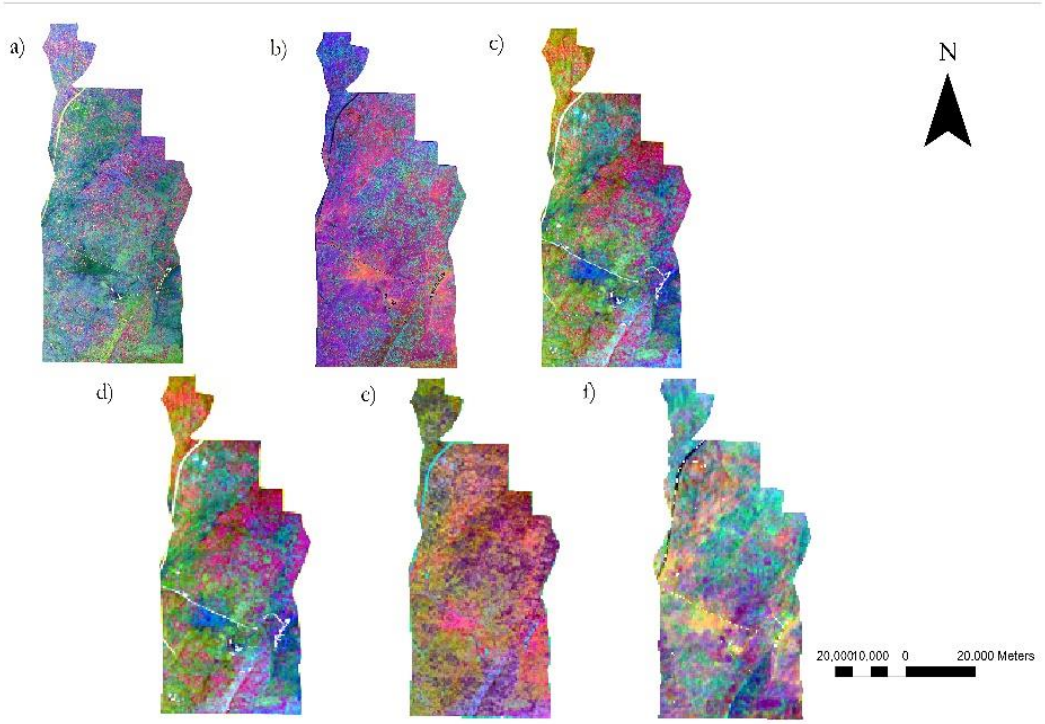

Figure 7 RGB combination using the first 3 PCA Images Derived from a) AVIRIS-NG (4m) b) Spectrally Upscaled Image (4m with 7 bands) c)Spatially Upscaled Image (16m) d)Spatially Upscaled image (30m) e) Simulated Landsat (30m with 7 bands) and f) Landsat 8 Image

4.2. Cluster Discrimination

This subsection highlights the spectral classes derived from cluster analysis using the selected Principal Components (PCs). Figure 8 presents the results of the cluster discrimination based on the maximum number of clusters (Table 2) identified in each image.

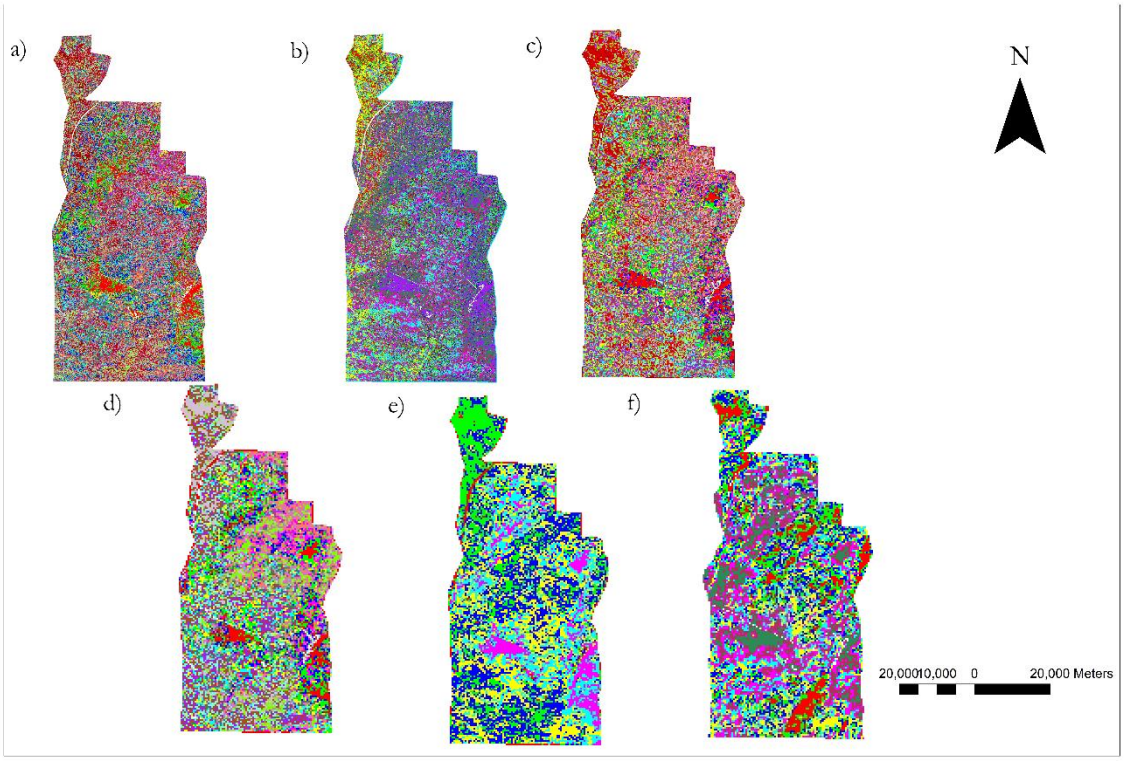

Figure 8 Spectral Classes generated using the classical k-means clustering for a) AVIRIS-NG (4m) b) Spectrally Upscaled Image (4m with 7 bands) c)Spatially Upscaled Image (16m) d)Spatially Upscaled image (30m) e) Simulated Landsat (30m with 7 bands) and f) Landsat 8 Image.

Table 2 Cluster Discrimination

Remote Sensing Data	AVIRIS-NG (4m)	Spectrally Upscaled Image (4m)	Spatially Upscaled 16m	Spatially Upscalled 30m	Simulated Landsat (30m)	Landsat (30m)
Cluster	18	9	18	16	6	8

Table 2 displays the pre-defined number of clusters obtained using the Davies Bouldin Index for each image. Among the considered images, it is worth noting that both the AVIRIS-NG image and the spatially upscaled 16m image exhibited the highest number of clusters in cluster discrimination (18), followed by the spatially upscaled 30m image (16), the spectrally upscaled 4m image (9), Landsat 8 (8) and lastly, the simulated Landsat (6). It is evident that most of the clusters are produced at high spatial and spectral resolution. The number of clusters can be seen from the spatially upscaled images (16m and 30m) to decrease as the spatial resolution is degraded. Additionally, the clusters in the spectrally upscaled image (4m) demonstrate how the spectral component affects cluster discrimination. It has been noted that the image loses its discrimination strength as the high spatial resolution (4m) is retained while the spectral

resolution degrades. Aside from that, the simulated multispectral Landsat image and the actual Landsat data produced a similar number of clusters, although slightly. Overall, the cluster discrimination signifies that the spatial component plays a more crucial role in discriminating clusters than the spectral component.

4.3. Corresponding Spectral curves

The spectral characteristics of the obtained clusters within each image were analyzed by deriving and plotting the average and standard deviation of the spectra of each cluster for visual examination. The average of all pixels allocated to that cluster serves as the centre and representative value of the cluster, shedding light on the general characteristics or behaviour of the cluster. The standard deviation of the cluster signifies how varied or similar the pixels are among a cluster. The visual examination of the average spectral profiles of the various clusters showed that there were clusters that did not belong to a vegetation class (a combination of dry vegetation and soil, while others were soil only). For the considered images, it was identified that: 13 out of the 18 clusters in AVIRIS-NG, 5 out 9 clusters in the spectrally upscaled 4m image, 14 clusters out of the 18 clusters in the spatially upscaled 16m image, 13 clusters out of the 16 clusters in the spatially upscaled 30m image, 4 out the 6 clusters in the simulated Landsat image, and the 5 out of the 8 clusters were identified not to be vegetation. Figure 21 to Figure 26 contain the respective spectral profiles for each image (i.e. AVIRIS-NG, spectrally upscaled (4m) image, spatially upscaled 16m image, spatially upscaled 30m image, simulated Landsat and Landsat 8).

4.3.1. Endmember Analysis

After estimating the mean spectral signatures in each cluster in the considered images, Spectral Feature Fitting (SFF) was conducted to examine the purity of the spectral traces of the clusters in the AVIRIS-NG that are similar to vegetation. On the other hand, the vegetation spectral classes from Landsat 8 were verified by deriving the correspondence between the very high resolution images and clusters. Figure 9 outlines the Spectral Feature Fitting (SFF) scores for AVIRIS-NG clusters.

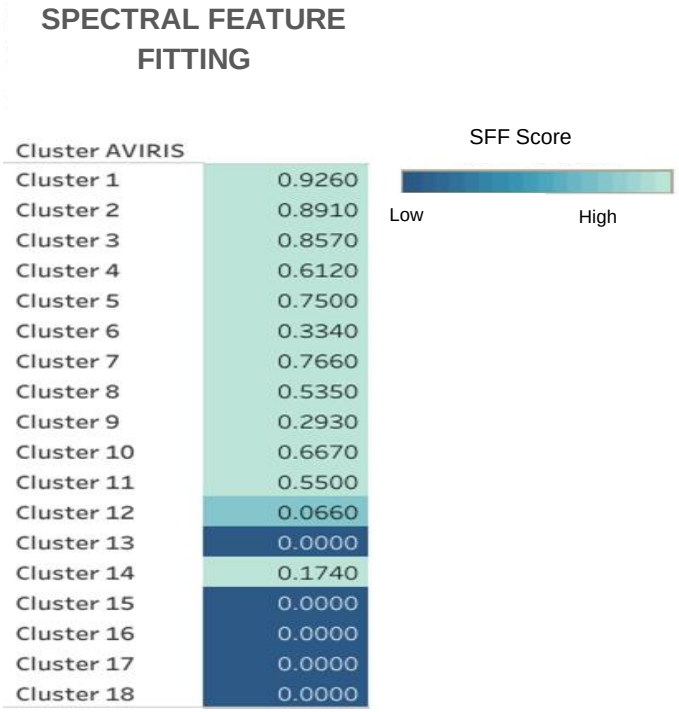

Figure 9 shows the SFF Score for Clusters in AVIRIS-NG derived by comparison with the AVIRIS vegetation spectral library. The shading intensity highlights the pure vegetation spectral profiles among the clusters.

As illustrated in Figure 9, Cluster 13, Cluster 15, Cluster 16, Cluster 17 and Cluster 18 (SFF scores of 0.0) indicate similarity to the endmember vegetation in the JPL AVIRIS spectral library. The colour intensity fades as the clusters are mixed with vegetation and other background information. Cluster 1 had the highest SFF score (0.926), indicating that the spectral profile is not vegetation. Figure 10 displays the spectral profiles of Cluster 13, Cluster 15, Cluster 16, Cluster 17 and Cluster 18, evidenced as vegetation species based on the SFF score and Cluster 1 identified not to be vegetation.

Furthermore, SFF also highlights the phenology of the vegetation species in the region as the time spot (summer), which is characterized by less rainfall and high temperature, causing the understorey (such as grasses) to be dry. The spectral profiles of the other clusters also indicate that the clusters can be affected by mixed reflectance of dry grasses and underlying soil reflectance. For instance, it is seen in clusters like Cluster 12 and Cluster 14 (Figure 47), which were slightly close to being pure vegetation had an influence of non-vegetative spectral signatures or background effects included in those regions.

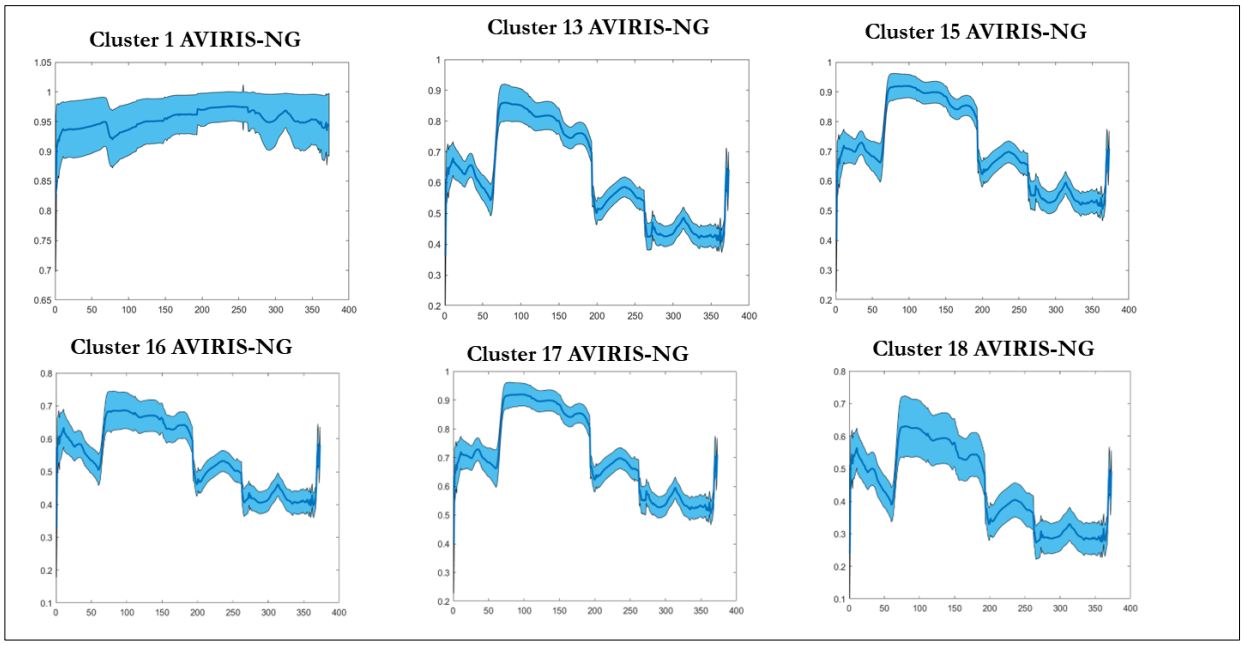

Figure 10 Spectral Signatures for .Cluster 13, Cluster 15, Cluster 16, Cluster 17 and Cluster 18.

According to Figure 11, three spectral profiles from the real Landsat 8 were identified as vegetation species (Cluster 3, Cluster 7, and Cluster 8). However, the remaining spectral profiles represented mixtures of non-vegetation elements (soil) and non-photosynthetic vegetation, while some were solely composed of soil. Landsat 8 clusters were geographically linked with high-resolution imagery for visual examination. Also, it was seen that the vegetation species in Landsat Cluster 7 were less dense than Landsat Cluster 8 and typically located around Landsat Cluster 8. Compared to AVIRIS-NG (4m), Landsat data shows that the lower spatial resolution makes the pixels more homogenous and detects less background information to form more clusters.

Additionally, the gamma diversity of SJER is evident through the Landsat data, showcasing the total variability in vegetation species within the study area.

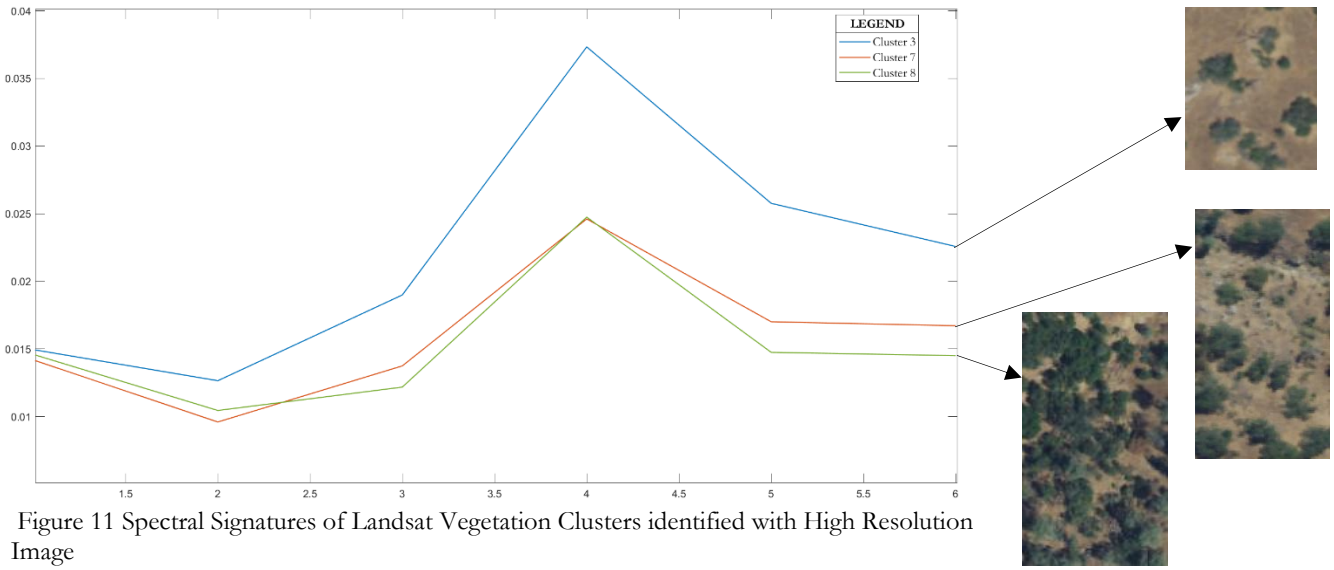

Figure 11 Spectral Signatures of Landsat Vegetation Clusters identified with High Resolution Image

4.4. Species Richness

For estimating species richness, spectral classes were treated as spectral species. This approach considers spectral diversity proxy for species diversity, where each spectral class represents one or more species that share similar spectral signatures. For example, a pixel in SJER might be composed of deciduous and evergreen oak (*Quercus douglesii, Quercus wislizeni*) or a combination of deciduous, grey pine and evergreen oak (*Quercus douglesii, Quercus wislizeni, Pinus sabiniana*) or bare soil only. Thus, spectral diversity is related to species diversity. A moving window of 100 by 100m was used to calculate species richness in each image. Considering the strong spectral diversity dependence on spatial resolution, larger pixel sizes (such as Landsat 8) had fewer pixels in the 1-ha moving window. Hence, fewer unique species are computed at lower spatial resolutions than at higher spatial resolutions. The surrounding pixels of the boundary area did not have enough pixels to fill a 1-hectare (ha) moving window due to the algorithm employed to estimate species richness. As a result, less than four species were recorded in those areas. Figure 12 below shows the resultant species richness maps for the real and simulated data.

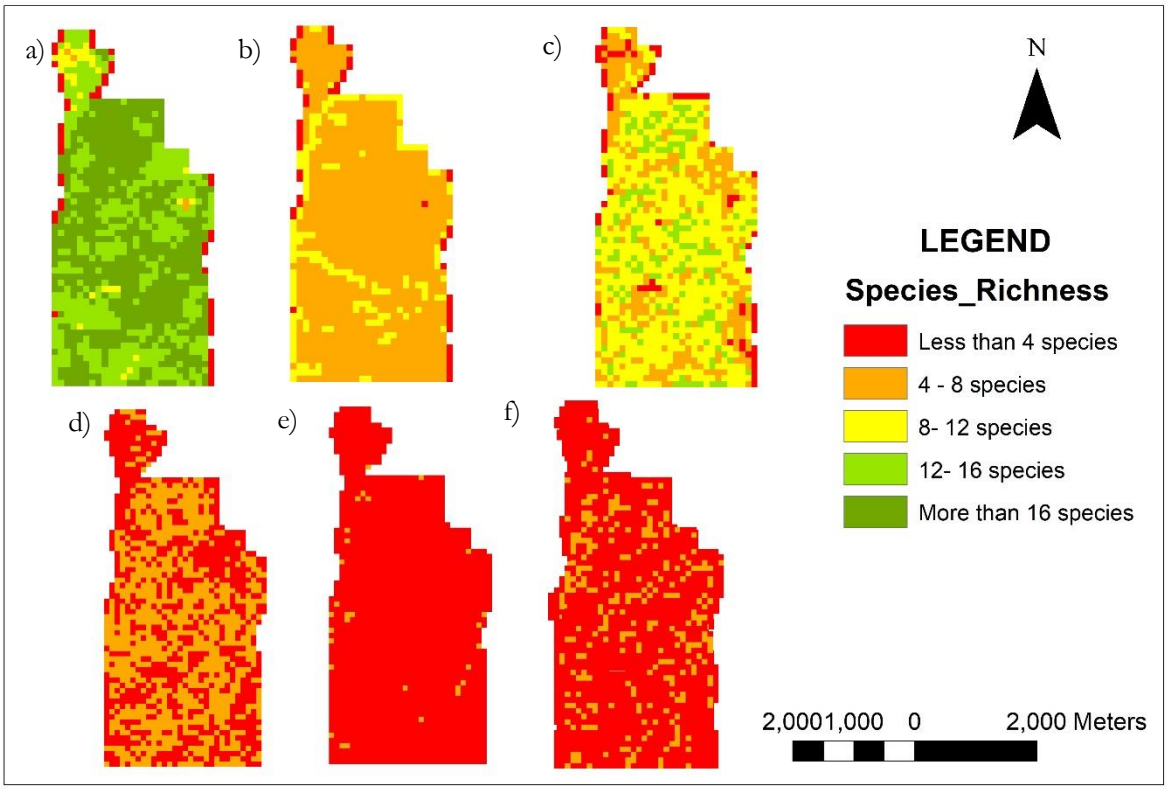

Figure 12 Species Richness a) AVIRIS-NG (4m) b) Spectrally Upscaled Image (4m with 7 bands) c)Spatially Upscaled Image (16m) d)Spatially Upscaled image (30m) e) Simulated Landsat (30m with 7 bands) and f) Landsat 8 Image.

From Figure 12, it can be seen that there is a reduction in the number of species as the image is being degraded spatially and spectrally. High spatial resolution images (i.e. AVIRIS-NG, spatially upscaled 16m, spectrally upscaled 4m) depicted more variation in the number of species than the images with a low spatial resolution (Spatially upscaled 30m, Simulated multispectral and Landsat 8 data). The spatially upscaled 16m image detected a higher variation of unique species compared to the spectrally upscaled image with a 4m resolution due to the higher spectral resolution found in the image to detect variation across the landscape. Similar to the Landsat data, the spatially upscaled 30m image also depicted a similar number of unique species (ranging from 4-8 species) in the study area. However, it is more evident that the 30m spatially

upscaled image shows a more pronounced presence of species between the range 4 to 8 species than in the Landsat 8 data. This is attributed to the high spectral component of the spatially upscaled image.

4.4.1. Spatial consistency

The spatial consistency of remote sensing images (spectrally upscaled 4m image, spatially upscaled 16m image, spatially upscaled 30m image, simulated Landsat, and Landsat) was examined in conjunction with AVIRIS-NG images to identify similarities between clusters following the species richness estimation. Figure 13 and Figure 15 show the identified spatially consistent clusters with AVIRIS with the respective spectral traces displayed in Figure 14 and Figure 16.

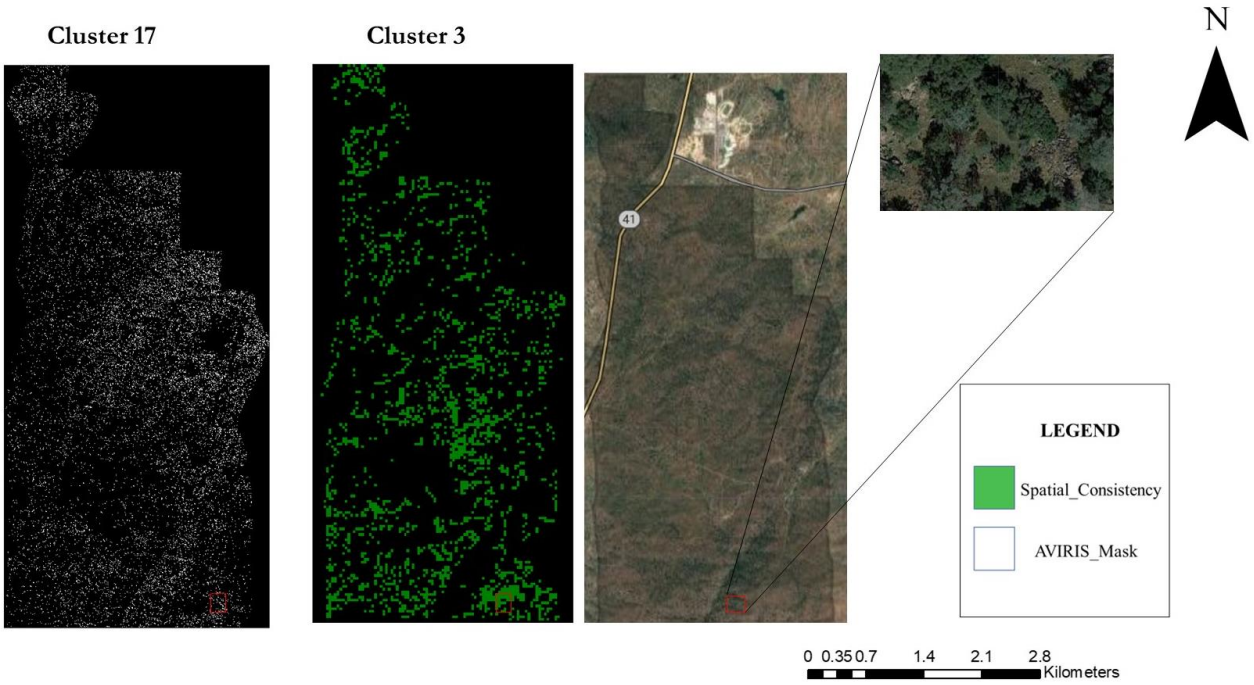

Figure 13 Spatially Consistent Clusters In Landsat And AVIRIS-NG Together with a Corresponding Region In High Resolution.

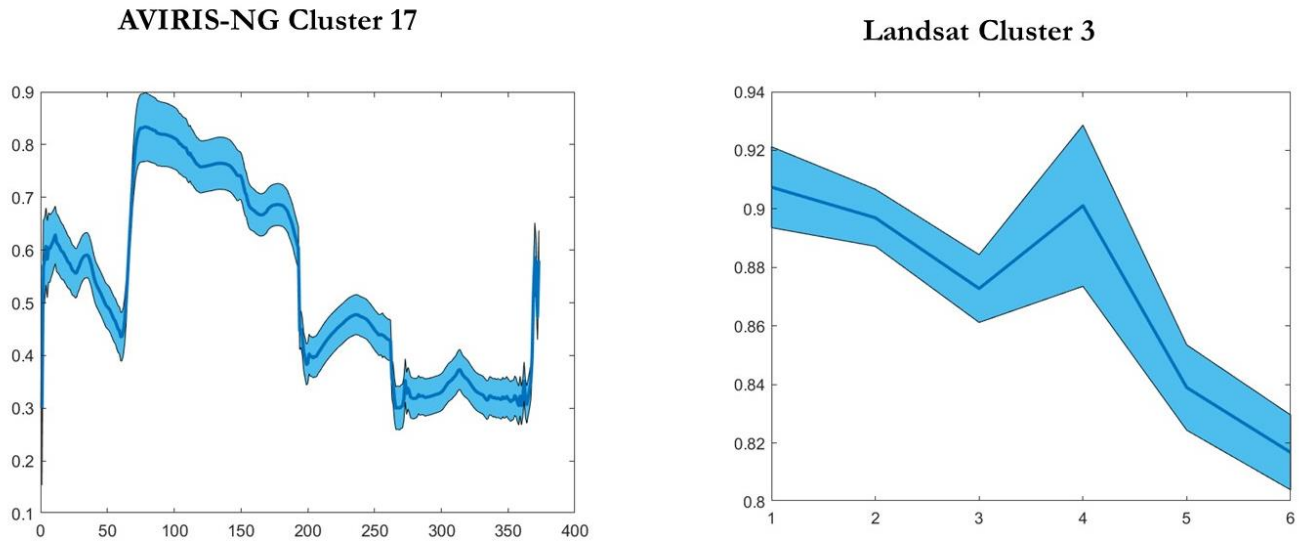

Figure 14 Corresponding Spectral Curves of AVIRIS Cluster 17 and Landsat Cluster 3.

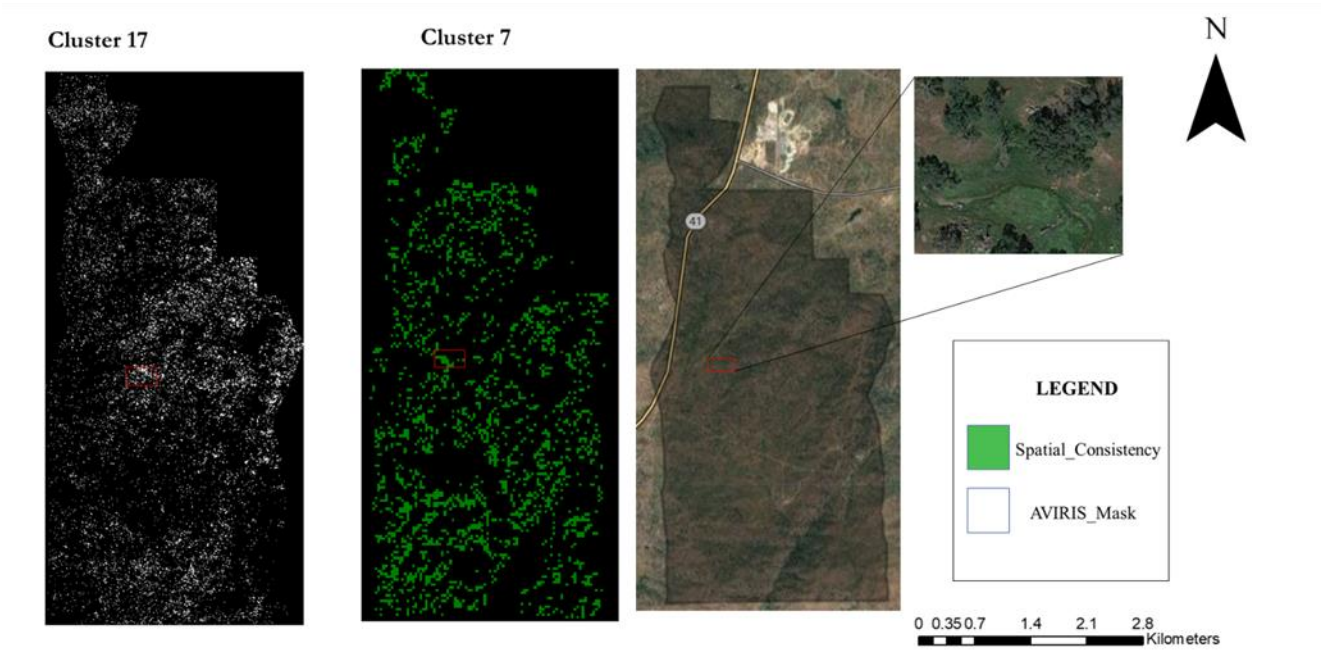

Figure 15 Spatially Consistent Clusters In Landsat And AVIRIS-NG Together with a Corresponding Region In High Resolution.

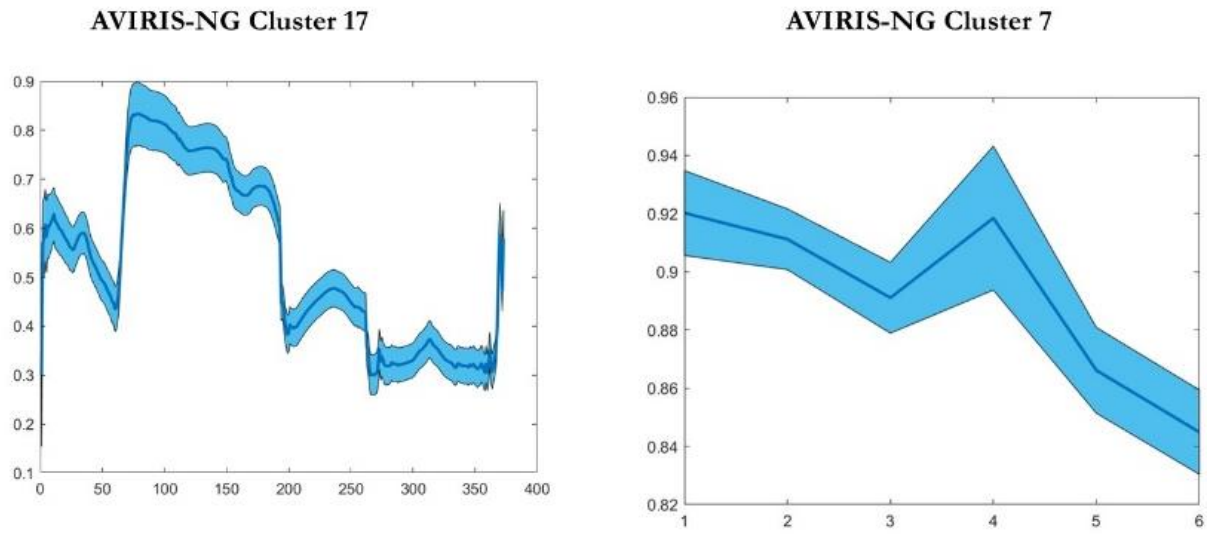

Figure 16 Corresponding Spectral Traces of AVIRIS Cluster 17 and Landsat Cluster 7.

Figure 13 showcases the clusters in AVIRIS-NG (Cluster 17) and Landsat 8 (Cluster 3) data identified to have a similar spatial pattern through visual examination. It can be seen that the spatially consistent cluster is vegetation based on the high resolution image included, as well as the spectral profiles provided in Figure 14.

Based on Figure 15, it is evident that Landsat cluster 7 exhibits a similar spatial pattern to AVIRIS-NG cluster 17. These spatially consistent clusters identified as vegetation correspond to the high resolution image. Also, Figure 16 provides the spectral signatures of the respective clusters that further support their classification as vegetation.

The identified clusters imply that vegetation species can be consistently and accurately characterized for comparison and analysis to understand species patterns and dynamics in the Landsat scene. The resulting spatial consistency of the remaining remote sensing images (Landsat, spatially upscaled 16m, spatially upscaled 30m, spectrally upscaled 4m and simulated Landsat) can be found in Figure 29 to Figure 46 in Appendix.

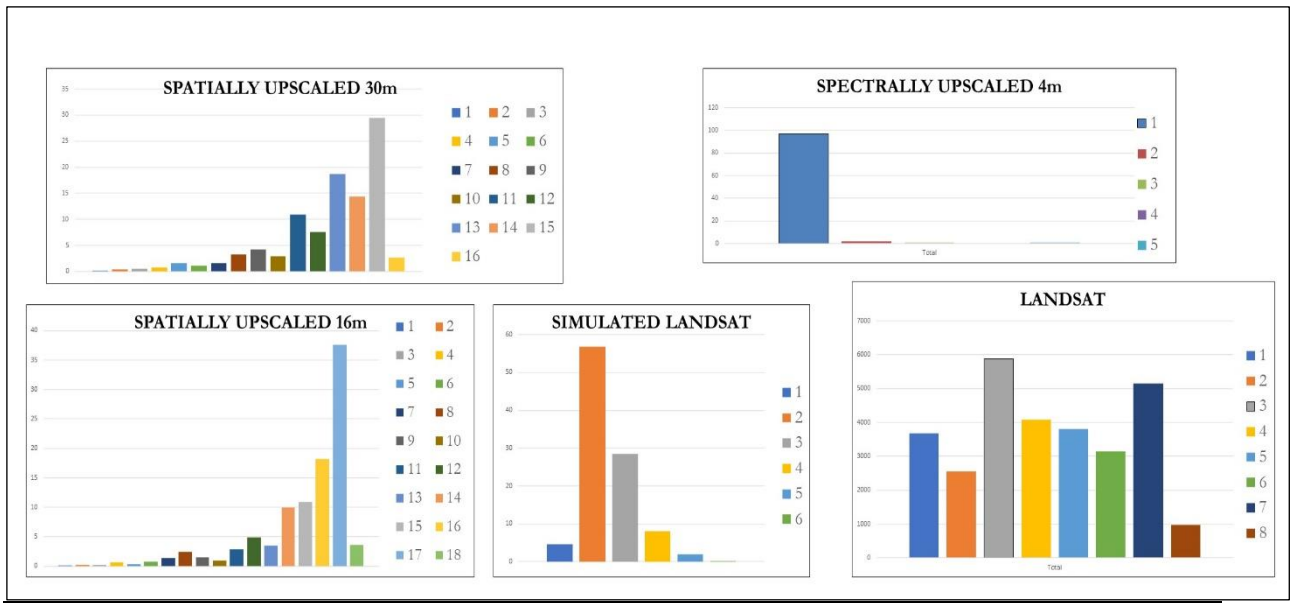

Figure 17 Frequency of Spatially Consistent Pixels Per Cluster with AVIRIS-NG.

Coupled with that, Figure 17 shows the number of pixels exhibiting spatial consistency with a cluster in AVIRIS-NG. The highest number of similar pixels with AVIRIS-NG are found in cluster 3 of Landsat (5883 pixels), cluster 15 (9631) of the spatially upscaled 30m, cluster 17 (12293) of the spatially upscaled 16m, cluster 2 (18715) of the simulated Landsat and cluster 1 (32271) of the spectrally upscaled 4m image.

4.4.2. Validation Results

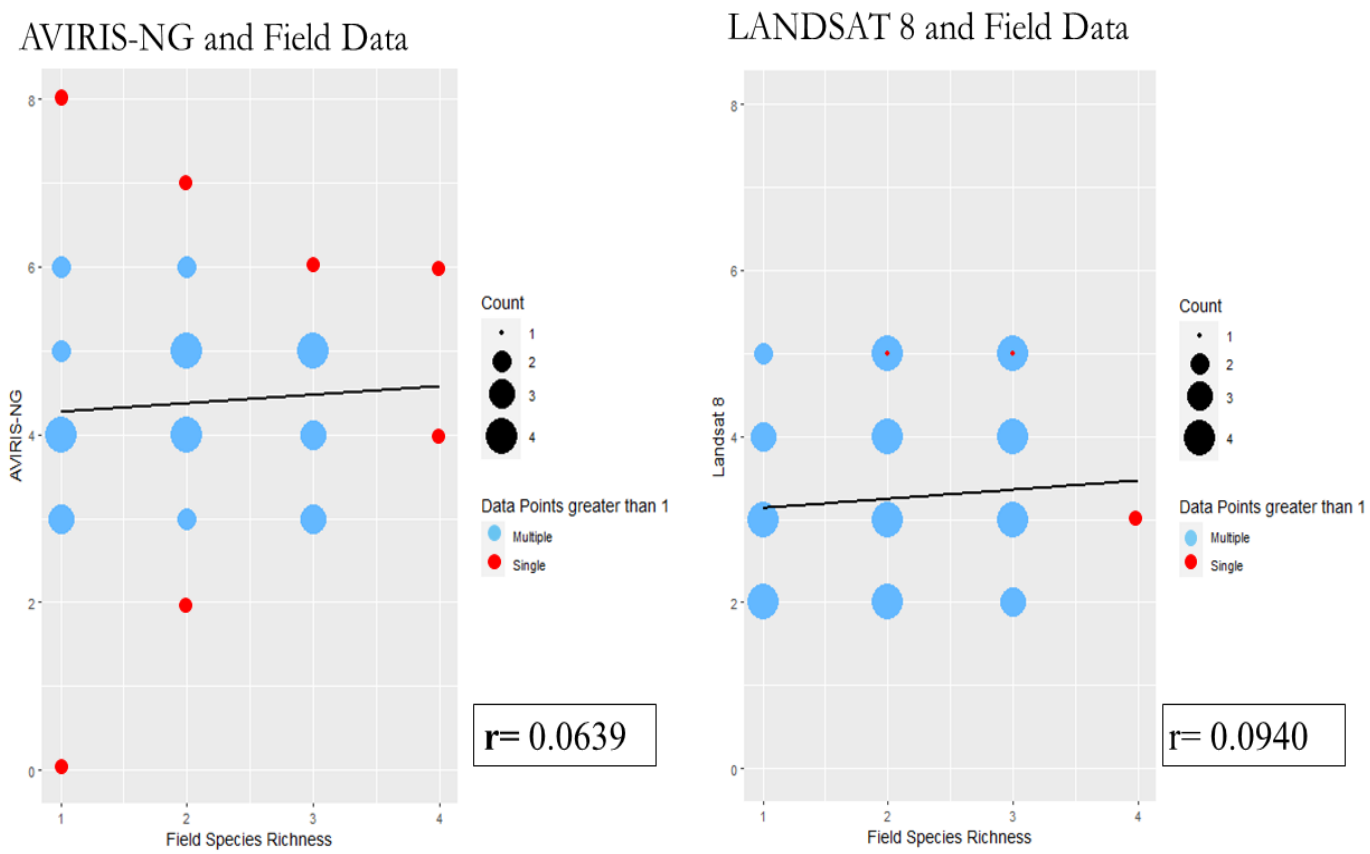

Figure 18 Correlation of the Landsat and AVIRIS-NG data with Field data with the number of points overlapped at a specific point location influences the size of the points in the figure.

Table 3 Correlation of Field Data with Open and Closed Forest

Remote Sensing Data	AVIRIS-NG	Spectrally Upscaled Image (4m)	Spatially Upscaled 16m	Spatially Upscaled 30m	Simulated Landsat	Landsat
Closed Forest	0.68	0.65	0.25	0.68	0.65	0.65
Open Forest	-0.068	0.5	-0.11	-0.068	0.21	0.01

Figure 18 depicts the correlation between the field data and Landsat 8 and AVIRIS-NG images; results show that the remote sensing images overestimated, albeit slightly. The point size increases with the number of overlapped points at a given location in the graph. 40 field plots in total were used for validation. Results indicate a low correlation between the species richness from field data and Landsat 8 data ($r^2 = 0.0940$) and

AVIRIS-NG data (r^2 = 0.0639). However, it is worth noting that Landsat 8 showed a relatively higher correlation compared to AVIRIS-NG.

Considering the correlation of the field data with the closed and open forests separately, Table 3 shows an overall improvement in the correlation between the closed forest and species richness field data than with the open forest, except for the spatially upscaled 16m image in the closed forest. The weak correlation in Figure 18 and the improved correlation in Table 3 corroborate the influence of background information when applying the SDH approach in SJER.

4.4.3. Spatial Pattern Analysis

This subsection focuses on the spatial pattern analysis conducted to pinpoint regions in the San Joaquin area with low biodiversity based on the species richness information obtained from the optical data.

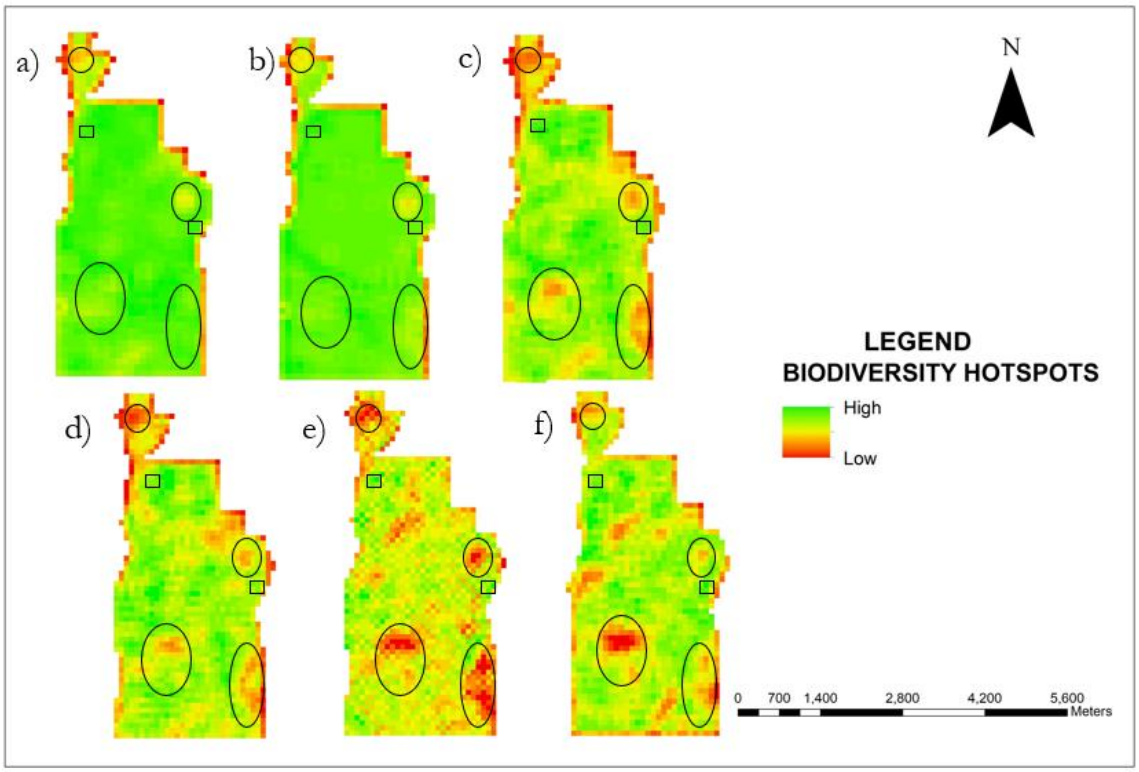

Figure 19 Comparative Analysis of Coldspot (black circles) and Hotspots (black squares) Patterns in a) AVIRIS-NG (4m) b) Spectrally Upscaled Image (4m with 7 bands) c)Spatially Upscaled Image (16m) d)Spatially Upscaled image (30m) e) Simulated Landsat (30m with 7 bands) and f) Landsat 8 Image)

Figure 19 demonstrates a consistent pattern of low-diversity areas (identified by black circles) across the optical images. The Getis Ord Gi * statistic in the ENVI software determined the coldspot areas in SJER across the considered images. This z-statistic revealed statistically significant (Table 4) spatial clusters of pixels. Coldspots – areas where low species richness levels are concentrated – were identified. The black-circled areas were determined coldspot and hotspot regions identified to have low biodiversity and are consistent across the optical images.

Table 4 Significant Test Result for the Optical Data

Optical Data	**Z-Score**
AVIIRS-NG	19.71
Spectrally Upscaled 4m	17.75
Spatially Upscaled 16m	20.57
Spatially Upscaled 30m	16.78
Simulated Landsat	15.40
Landsat 8	14.58

The z-scores in Table 4 indicate the level of statistically significant pattern in the respective optical data (AVIIRS-NG, Spectrally Upscaled 4m, Spatially Upscaled 16m, Spatially Upscaled 30m, Simulated Multispectral, and Landsat 8). The spatially upscaled 16m data has the highest z-score of 20.57, indicating a highly significant result. AVIRIS-NG data follows closely with a z-score of 19.71, indicating a highly significant result. The spectrally upscaled 4m image has a significant result with a z-score of 17.75, although slightly lower than AVIRIS-NG. The spatially upscaled 30m image shows a significant result with a z-score of 16.78. The simulated Landsat image has a z-score of 15.40, indicating a significant result, albeit lower than the previous datasets. Finally, Landsat 8 data has a z-score of 14.58, which is relatively lower than the other datasets but still signifies a significant result. This finding underscores the importance of upscaling spatial resolution when analyzing spatial patterns in the Mediterranean region.

.

5. .DISCUSSION

This section of the research reflects on the findings derived from the analysis conducted in this study.

5.1. Spectral Diversity Hypothesis and its Application in the Meditterean Ecosystem

Hyperspectral data has proven helpful in applying the SDH approach in areas with high species variability, such as the dense tropical forest (Féret & Asner, 2014) areas where background information such as soils had been effectively masked out. However, this phenomenon did not occur in the Mediterranean ecosystem, such as SJER. This study represents one of the first real-world applications of SDH with low vegetation cover in the Mediterranean ecosystem with strong influence from the soil. With low vegetation, additional care is required in filtering out non-vegetative information in the Mediterranean ecosystem.

In the case of the dimensionality reduction using PCA, it was observed that the spectral domain of NIR and SWIR were the most significant in contributing to the PCs in real data and simulated data for estimating spectral heterogeneity. This finding aligns with numerous studies that indicate the pronounced synergy reflectance at the canopy level in the near-infrared (NIR) region as well as the additional information provided by the SWIR region in capturing biochemical and structural traits in vegetation for differentiating vegetation species (Estornell et al., 2013; Hall et al., 2012; Heumann et al., 2015; Madonsela et al., 2017b; Ollinger, 2011). The variables (bands) that cause the most variance represent the primary construct of the spectral feature space (Sousa & Small, 2018). The similarity in the regions contributing to the principal components of AVIRIS-NG and Landsat data shows that the multispectral data represents the fundamental vegetation species structure found in the AVIRIS-NG image despite the AVIRIS-NG image reflecting a variety of spectral information indistinguishable from the Landsat data.

Using SFF (Figure 9) and from visual exploration in the Landsat data (Figure 11), it was determined that the vegetation species in SJER were more than three (3). The study concurs with previous studies by Newman & Duncan (1973), noting that the least number of tree species in SJER is 3. To add to this, the findings of this study should not be interpreted to suggest that the hyperspectral data cube from AVIRIS-NG data is limited to detecting four or five different vegetation species. Similarly, it should not be assumed that multispectral (Landsat) can capture the same data as the AVIRIS-NG data cube. Instead, the study shows that both datasets exhibit a comparable number of fundamental dimensions and a similar geometric relationship among their spectra when linearly decomposed using PCA.

The high number of (18) clusters in the AVIRIS-NG images may ascribe to the subtle variations in pixel values amplified due to the high spatial and spectral resolution of AVIRIS-NG. This over-segmentation may also have slightly overestimated the species richness results by producing too many small clusters, particularly in open forest areas where background information is present. For instance, in viewing the AVIRIS-NG image and its corresponding images (PCA and RGB) in Figure 20, it is evident that there is an overestimation of the clusters in the AVIRIS-NG image, where more than one cluster was produced on a canopy crown. This finding is consistent with Griffith et al (2021), who noted that redundant information could be introduced into images of the Mediterranean ecosystem at fine resolution. However, it is observed from the study that there may be other species not captured in the dominant classifications. On the other hand, the overestimation in the AVIRIS-NG can be attributed to the nature of species found in SJER. According to Roth et al (2015), the classification of coniferous species, such as grey pines (*Pinus Sabiniana*) in the southern Sierra Nevada region, proved challenging due to the intensive mixture at fine resolution. This is because these species occur as unique clusters of individual species during classification. To add to

that, the herbaceous species are known to be very dry in the summer due to their response to low soil moisture and high temperature.

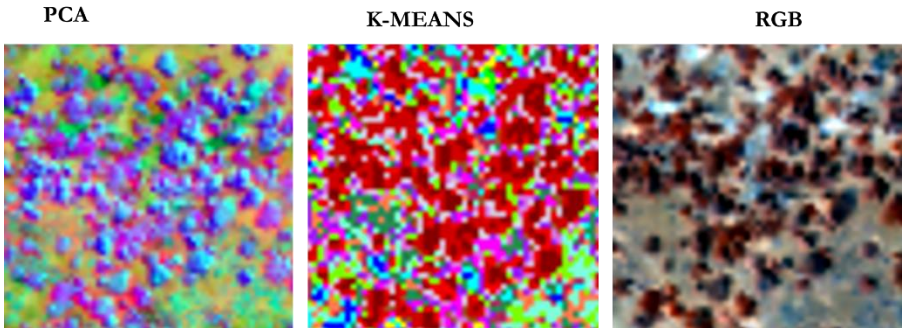

Figure 20 Overestimation in AVIRIS-NG.

5.2. Spectral Diversity in Upscaled Hyperspectral Data

It can be observed in Table 2 that spatial resolution strongly influences the discrimination of clusters in the study area, which consequently affects species richness estimations. It is observed that as the AVIRIS-NG (4m) image is spatially upscaled to 16m resolution and 30m resolution separately, there is a slight reduction in cluster discrimination from 18 clusters in the spatially upscaled 16m image to 16 clusters in the spatially upscaled 30m image.

A decrease in spatial resolution can impact spectral mixing, affecting the optimal number of spectral species in k-means clustering. The spatial upscaling of the AVIRIS-NG reduces the detail of spectral reflectances from the San Joaquin area. Furthermore, it was observed that both the simulated multispectral data and Landsat 8 data showed the lowest number of unique species (Table 2). This is attributed to the low spatial resolution (30m) of multispectral data affecting the capacity to detect distinct spectral signals in vegetation (Badola et al., 2022). It also results in fewer pixels within the 1 ha moving window used in estimating species richness compared to AVIRIS-NG.

Conversely, it was observed in the spatially upscaled 30m image and Landsat data that spectral resolution plays a role in estimating species richness. The Landsat data and simulated multispectral Landsat distinguished 8 and 6 clusters, respectively, while the spatially upscaled 30m data detected 16 clusters in the region. Additionally, it was observed in the spectrally 4m upscaled image that despite the high spatial resolution detected, only 9 clusters could be discriminated. However, its small pixel size makes it possible for more pixels in the 1 ha moving window compared to the 30m resolution images, making it a slightly higher species richness compared to the simulated multispectral and Landsat data, as shown in Figure 12. Finally, the results in Table 2 showed that the high spectral resolution in the spatially upscaled 16m and 30m resolution helped to detect subtle variations in the area resulting in a higher species richness being measured in SJER, as seen in Figure 12.

5.3. Comparison of Performance in AVIRIS-NG and Multispectral Data

In contrast to earlier studies conducted by Féret & Asner (2014), Hall et al. (2012) and Rocchini et al. (2015), this research revealed an overall weaker correlation (R^2 of 0.0639 in AVIRIS-NG and R^2 of 0.0940 in Landsat) between species richness and species diversity. Nevertheless, the study discovered that the higher accuracy of the closed forest was consistent with previous studies regardless of the weaker overall correlation. According to Table 3, the R^2 values of the closed forest range from 0.25 to 0.68. These R^2 values can be deemed valid for species diversity from spectral variation, as Rocchini et al. (2015) stated that R^2 values are

considered valid for species diversity from spectral variation. Furthermore, implementing methods to mask out non-vegetative pixels in the San Joaquin area for both open and closed forest areas would provide an efficient approach to assessing vascular species in the Mediterranean region. Besides, there was a low correlation between species richness in open forests and species richness in field data due to background information (soil and dry vegetation) affecting the spectral classes used to assess species richness. The low correlation between the field data and the Landsat 8 and AVIRIS-NG images can be attributed in part to the characteristics of the Mediterranean ecosystem being predominantly an open woodland.

There is a need to consider appropriate sensor resolution based on the characteristics of the landscape features of interest to ensure optimal spectral information capture (Sousa & Small, 2018). The comparison of the R^2 values between Landsat 8 (0.65) and AVIRIS-NG (0.68) in Table 3 shows the potential of Landsat data in estimating species diversity in the San Joaquin Experimental Range (SJER). With the landscape features of SJER compared to tropical areas, Landsat 8 data, with its lower spatial and spectral resolution, captures a heterogenous mixture of spectra with lesser background detail and produces optimal variation in spectral patterns. This can effectively map species diversity given that there are fewer species in the region as compared to the tropical areas that require high-fidelity image spectroscopy to map biodiversity. This finding aligns with the study conducted by Viedma et al. (2012), who argued that using multispectral sensors in conjunction with large sampling plot sizes (greater than 100 m2) allowed for high accuracy prediction of overall species richness in the Mediterranean region of Spain.

5.4. Consistency of Spatial Patterns and Relationships

Despite the differences in spectral and spatial resolutions in measuring species richness in San Joaquin, the spatial patterns of vegetation species between clusters remained consistent across the dataset, even in the spatially and spectrally upscaled AVIRIS-NG images. The spectral similarities of the spatially consistent clusters in the Landsat 8 and AVIRIS-NG image imply that multispectral and hyperspectral feature spaces have comparable structures for measuring alpha diversity in the Mediterranean ecosystem, although AVIRIS-NG has high data dimensionality. The consistency of the spatial patterns in clusters in Landsat and AVIRIS-NG data has the capabilty to significantly inform analyses in studies where spatially or temporally limited hyperspectral information can complement the plethora of multispectral observations.

Aside from that, spatial pattern analysis was useful in detecting cold spots (areas of low species richness) in biodiversity for both the real and simulated data. This analysis was adapted from Boori et al. (2021), which used the Getis Ord Gi* statistic to identify vulnerable areas in a spatiotemporal ecological analysis. The consistent pattern of biodiversity cold spots shown in both real and simulated data signified the effect of environmental filtering.

5.5. Limitations

Applications of SDH using Landsat and AVIRIS-NG demonstrated its limits when applied to the Mediterranean ecosystem. Given that the images were captured during one of the driest years in the history of California (Huesca et al., 2021) and considering the nature of the vegetative species, especially the understorey being dry and also mixed with soil at that time in SJER, automatically masking out of non-vegetative pixels using the NDVI threshold (< 0.3) only was a challenge. In order to curb this limitation, non-vegetative pixels were masked out manually, as the automated method excluded important vegetative

areas in the study area. These vegetative areas were identified from high resolution images from the same time spot. Although these non-vegetative areas were attempted to be excluded, not all areas were detected.

Additionally, a challenge that was not considered in this study was the influence of topographic effects, such as aspect and shadows, in the spectral species estimations. For example, a north-facing species may exhibit slightly different spectral reflectance compared to a south-facing species of the same species due to the differences in sun exposure. These effects can result in the overestimation of species in the optical data. To mitigate this challenge, band normalization was performed to reduce the influences of these factors. For instance, since shadows reflect lower signals in the VNIR region, the bands with very low signals are adjusted to the lower limit to minimize the effect of all these errors.

Lastly, the field data used in this study was not explicitly collected for validating species richness estimates but for a slightly different purpose. Plots dominated by deciduous, annual or perennial trees were mainly sampled to depict their temporal evolution throughout the years.

5.6. Implications for Biodiversity Assessment

The Spectral Diversity Hypothesis, as proposed by Palmer et al. (2002), allows conservationists to map ecological conditions in the Mediterranean ecosystem using multispectral sensors, such as Landsat and Sentinel 2, rather than hyperspectral sensors. This method can help to detect areas where environmental conditions are unfavourable or less suitable for certain species to be intervened, given that Mediterranean areas are noted for drought and frequent fire outbreaks (Huesca et al., 2021; Ullrich et al., 2018).

Utilizing openly accessible multispectral data allows for consistent monitoring of the species to mitigate the effect of biodiversity loss through anthropogenic activities in the Mediterranean ecosystem. Hence, this is a cost-effective method of assessing biodiversity and will improve the ability to respond to biodiversity loss.

Additionally, this approach offers a stepping stone to monitor the temporal development and dynamics of species diversity at the pixel level using tailored indicators and Essential Biodiversity Variables (EBVs). With applications such as Breaks For Additive Seasonal and Trend (BFAST) together with the Box -Jenkins method, trends, seasonality, abrupt changes and emerging needs of the species can be predicted and forecasted by analyzing the spectral diversity in time. The Autoregressive Integrated Moving Average (ARIMA) model has been evidenced to have exceptional evaluations in demonstrating patterns in biodiversity as well as the trend of changes over an average time of years for the Mediterranean region (Martinez, 2012).

Although the SDH approach does not give details of specific species, it can offer valuable insights into the spatial pattern of biodiversity for sustainable management of the environment.

6. RECOMMENDATIONS AND CONCLUSION

The section of this study concludes with a summary of findings based on the analysis obtained from the real and simulated data and makes recommendations for further study.

6.1. Summary

This study was primarily aimed at applying the Spectral Diversity Hypothesis (SDH) in assessing biodiversity in the Mediterranean ecosystem. The research investigated the potential of different sensors, which were hyperspectral data from AVIRIS-NG, multispectral sensor Landsat 8, as well as spatially upscaled and spectrally upscaled AVIRIS-NG products, in estimating species richness using the same SDH method.

In general, it was observed that there was a weak correlation ($R^2 = 0.0639$ for AVIRIS and $R^2 = 0.0940$ for Landsat 8 data) between spectral diversity and species diversity in the region. This was attributed to the SJER being an open woodland with non-photosynthetically active vegetation and the influence of soil. However, it was revealed that the closed forest areas in the region presented a relatively higher accuracy of R^2 of 0.65 for Landsat, with AVIRIS-NG having an accuracy of R^2 of 0.68.

The discrimination of clusters in the spatially and spectrally upscaled AVIRIS-NG images revealed that the spatial component had a higher influence on the discrimination of clusters for estimating alpha diversity than the spectral component. The Landsat 8 data was able to discriminate vegetation species with a reduced effect of background information compared to AVIRIS-NG. This shows that although the high spectral resolution aids in discriminating species, the spatial component plays a crucial role. This study also revealed that out of the 18 clusters derived for the AVIRIS-NG image, only 5 clusters of pure vegetation species (SFF score of 0), whilst the other clusters were influenced by soil. Similar findings were observed in the Landsat data, where 3 clusters were detected as vegetation from visual exploration.

This study has shown that multispectral sensors effectively assess biodiversity in the Mediterranean ecosystem. This includes consistencies in spatial patterns of clusters as well as identified low biodiversity areas between AVIRIS-NG data (renowned for estimating species diversity due to its high spatial and spectral resolution) and Landsat data. Furthermore, the Principal Component Analysis revealed that the PCs were primarily influenced by bands in the NIR and SWIR regions in both AVIRIS-NG and Landsat 8.

6.2. Recommendations

This research serves as a springboard for additional studies into the application of SDH with the Mediterranean climate. To ensure the usability of the hyperspectral imagery when applying the SDH approach, non-vegetative and non-photosynthetically active vegetative pixels should be extensively masked out in the open forest areas to improve the accuracy in estimating species diversity since the Mediterranean areas are characterised mainly by open forest areas, dominated by shrubs, herbaceous plants, grasses with a higher influence of background information.

Aside from this, it is recommended to further investigate the application of the SDH extrapolated in the Mediterranean closed forest area, even though the closed forest areas showed a better accuracy compared to the overall study area by proving a higher correlation of species richness to species diversity.

Lastly, it will be beneficial to include the temporal component in the classification to improve discrimination from the soil and model the phenological pattern of understorey vegetation when applying the SDH approach for monitoring.

6.3. Conclusion

The portability of the SDH method ensures its usability and reliability in ecological areas; however, the context of the landscape should be taken into consideration. These findings are encouraging as they suggest that similar classification analyses can be applied to larger areas using emerging hyperspectral satellite imagery. Landsat can still effectively differentiate spectral classes that represent the environmental heterogeneity in the study area as well as detect spatially consistent areas as with the high spectral resolution images.

LIST OF REFERENCES

Aljunid, M. F., & Manjaiah, D. H. (2021). Data Management, Analytics and Innovation. In *Proceedings of ICDMAI* (Vol. 70). http://link.springer.com/10.1007/978-981-13-1402-5%0Ahttps://link.springer.com/10.1007/978-981-16-2934-1

Anand, A., Malhi, R. K. M., Srivastava, P. K., Singh, P., Mudaliar, A. N., Petropoulos, G. P., & Kiran, G. S. (2022). Optimal band characterization in reformation of hyperspectral indices for species diversity estimation. *Physics and Chemistry of the Earth*, *126*(March 2021), 103040. https://doi.org/10.1016/j.pce.2021.103040

Badola, A., Panda, S. K., Roberts, D. A., Waigl, C. F., Jandt, R. R., & Bhatt, U. S. (2022). A novel method to simulate AVIRIS-NG hyperspectral image from Sentinel-2 image for improved vegetation/wildfire fuel mapping, boreal Alaska. *International Journal of Applied Earth Observation and Geoinformation*, *112*(July), 102891. https://doi.org/10.1016/j.jag.2022.102891

Banskota, A., Kayastha, N., Falkowski, M. J., Wulder, M. A., Froese, R. E., & White, J. C. (2014). Forest Monitoring Using Landsat Time Series Data: A Review. *Canadian Journal of Remote Sensing*, *40*(5), 362–384. https://doi.org/10.1080/07038992.2014.987376

Boori, M. S., Choudhary, K., Paringer, R., & Kupriyanov, A. (2021). Spatiotemporal ecological vulnerability analysis with statistical correlation based on satellite remote sensing in Samara, Russia. *Journal of Environmental Management*, *285*(July 2020), 112138. https://doi.org/10.1016/j.jenvman.2021.112138

Buotte, P. C., Law, B. E., Ripple, W. J., & Berner, L. T. (2020). Carbon sequestration and biodiversity co-benefits of preserving forests in the western United States. In *Ecological Applications* (Vol. 30, Issue 2). https://doi.org/10.1002/eap.2039

Cardinale, B. J., Duffy, J. E., Gonzalez, A., Hooper, D. U., Perrings, C., Venail, P., Narwani, A., MacE, G. M., Tilman, D., Wardle, D. A., Kinzig, A. P., Daily, G. C., Loreau, M., Grace, J. B., Larigauderie, A., Srivastava, D. S., & Naeem, S. (2012). Biodiversity loss and its impact on humanity. *Nature*, *486*(7401), 59–67. https://doi.org/10.1038/nature11148

Chao, A., & Chiu, C.-H. (2016). Species Richness: Estimation and Comparison. *Wiley StatsRef: Statistics Reference Online*, 1–26. https://doi.org/10.1002/9781118445112.STAT03432.PUB2

Chiarucci, A., Bacaro, G., & Scheiner, S. M. (2011). Old and new challenges in using species diversity for assessing biodiversity. *Philosophical Transactions of the Royal Society B: Biological Sciences*, *366*(1576), 2426–2437. https://doi.org/10.1098/rstb.2011.0065

Colwell, R. K., & Coddington, J. A. (1994). Estimating terrestrial biodiversity through extrapolation. *Philosophical Transactions of the Royal Society of London. Series B, Biological Sciences*, *345*(1311), 101–118. https://doi.org/10.1098/rstb.1994.0091

Comiskey, J. A., Ayzanoa, G. E., & Dallmeier, F. (1995). A data management system for monitoring forest dynamics. *Journal of Tropical Forest Science*, *7*(3), 419–427.

Commission, F. A. O., Genetic, O. N., & For, R. (2019). The State of the World's Biodiversity for Food and Agriculture. In *The State of the World's Biodiversity for Food and Agriculture*. https://doi.org/10.4060/ca3129en

Cowling, R. M., Rundel, P. W., Lamont, B. B., Arroyo, M. K., & Arianoutsou, M. (1996). Plant diversity in mediterranean-climate regions. *Trends in Ecology and Evolution*, *11*(9), 362–366. https://doi.org/10.1016/0169-5347(96)10044-6

Davies, D. L., & Bouldin, D. W. (1979). A Cluster Separation Measure. *IEEE Transactions on Pattern Analysis and Machine Intelligence*, *PAMI-1*(2), 224–227. https://doi.org/10.1109/TPAMI.1979.4766909

Dornelas, M., Gotelli, N. J., McGill, B., Shimadzu, H., Moyes, F., Sievers, C., & Magurran, A. E. (2014). Assemblage time series reveal biodiversity change but not systematic loss. *Science*, *344*(6181), 296–299. https://doi.org/10.1126/science.1248484

Dronova, I., & Taddeo, S. (2022). Remote sensing of phenology: Towards the comprehensive indicators of plant community dynamics from species to regional scales. *1460 | Journal of Ecology*, *110*, 1460–1484. https://doi.org/10.1111/1365-2745.13897

El Abbassi, M., Overbeck, J., Braun, O., Calame, M., van der Zant, H. S. J., & Perrin, M. L. (2021). Benchmark and application of unsupervised classification approaches for univariate data. *Communications Physics*, *4*(1), 1–9. https://doi.org/10.1038/s42005-021-00549-9

Estornell, J., Martí-Gavliá, J. M., Sebastiá, M. T., & Mengual, J. (2013). Principal component analysis applied to remote sensing. *Modelling in Science Education and Learning*, *6*, 83. https://doi.org/10.4995/MSEL.2013.1905

Féret, J. B., & Asner, G. P. (2014). Mapping tropical forest canopy diversity using high-fidelity imaging spectroscopy. *Ecological Applications*, *24*(6), 1289–1296. https://doi.org/10.1890/13-1824.1

Fernandez-Bou, A. S. (UC M., Ortiz-Partida, J. P. (UC M., Classen- Rodriguez, L. (Saint L. U., & Espinoza, V. (UC M. (2022). *Introduction to California ' s Fourth Climate Change Assessment. San Joaquin Valley Region Report. M*.

Fettig, C. J., Wuenschel, A., Balachowski, J., Butz, R. J., Jacobsen, A. L., North, M. P., Ostoja, S. M., Pratt, R. B., & Standiford, R. B. (2019). Managing Effects of Drought in California. *In: Vose, James M.; Peterson, David L.; Luce, Charles H.; Patel-Weynand, Toral, Eds. Effects of Drought on Forests and Rangelands in the United States: Translating Science into Management Responses. Gen. Tech. Rep. WO-98. Washington, DC: US Department Of*, *December*, 71–93.

Foerster, S., Carrère, V., Rast, M., & Staenz, K. (2016). *remote sensing Preface: The Environmental Mapping and Analysis Program (EnMAP) Mission: Preparing for Its Scientific Exploitation*. https://doi.org/10.3390/rs8110957

Gao, B. C., Heidebrecht, K. B., & Goetz, A. F. H. (1993). Derivation of scaled surface reflectances from AVIRIS data. *Remote Sensing of Environment*, *44*(2–3), 165–178. https://doi.org/10.1016/0034-4257(93)90014-O

Gauquelin, T., Michon, G., Joffre, R., Duponnois, R., Génin, D., Fady, B., Bou Dagher-Kharrat, M., Derridj, A., Slimani, S., Badri, W., Alifriqui, M., Auclair, L., Simenel, R., Aderghal, M., Baudoin, E., Galiana, A., Prin, Y., Sanguin, H., Fernandez, C., & Baldy, V. (2018). Mediterranean forests, land use and climate change: a social-ecological perspective. *Regional Environmental Change*, *18*(3), 623–636. https://doi.org/10.1007/s10113-016-0994-3

Gondwe, G. (2019). *Eradicating Rural Poverty to Implement the 2030 Agenda for Sustainable Development, Addis Ababa, 27. March*, 1–13.

Griffith Daniel M., Byrd Kristin B, Anderegg Leander DL, Allan Elijah , Gatziolis Demetrios , Roberts Dar, Yacoub Rosie, N. R. R. (2021). *Capturing patterns of evolutionary relatedness with reflectance spectra to model and 2 monitor biodiversity*. 1–29.

Hall, K., Reitalu, T., Sykes, M. T., & Prentice, H. C. (2012). Spectral heterogeneity of QuickBird satellite data is related to fine-scale plant species spatial turnover in semi-natural grasslands. *Applied Vegetation Science*, *15*(1), 145–157. https://doi.org/10.1111/j.1654-109X.2011.01143.x

Heumann, B. W., Hackett, R. A., & Monfils, A. K. (2015). Testing the spectral diversity hypothesis using spectroscopy data in a simulated wetland community. *Ecological Informatics*, *25*, 29–34. https://doi.org/10.1016/j.ecoinf.2014.10.005

Heymann, Ś., Latapy, M., & Magnien, C. (2012). Outskewer: Using skewness to spot outliers in samples and time series. *Proceedings of the 2012 IEEE/ACM International Conference on Advances in Social Networks Analysis and Mining, ASONAM 2012*, 527–534. https://doi.org/10.1109/ASONAM.2012.91

Huesca, M., Merino-de-Miguel, S., Eklundh, L., Litago, J., Cicuéndez, V., Rodríguez-Rastrero, M., Ustin, S. L., & Palacios-Orueta, A. (2015). Ecosystem functional assessment based on the "optical type" concept and self-similarity patterns: An application using MODIS-NDVI time series autocorrelation. *International Journal of Applied Earth Observation and Geoinformation*, *43*, 132–148. https://doi.org/10.1016/j.jag.2015.04.008

Huesca, M., Ustin, S. L., Shapiro, K. D., Boynton, R., & Thorne, J. H. (2021). Detection of drought-induced blue oak mortality in the Sierra Nevada Mountains, California. *Ecosphere*, *12*(6). https://doi.org/10.1002/ecs2.3558

IISD. (2019). *Policy Brief: Why Biodiversity Matters: Mapping the Linkages between Biodiversity and the SDGs | SDG Knowledge Hub | IISD*. https://sdg.iisd.org/commentary/policy-briefs/why-biodiversity-matters-mapping-the-linkages-between-biodiversity-and-the-sdgs/

International Union for Conservation of Nature Red List of Threatened Species. (2021). *IUCN Red List of Threatened Species*. https://www.iucnredlist.org/

Isbell, F., Adler, P. R., Eisenhauer, N., Fornara, D., Kimmel, K., Kremen, C., Letourneau, D. K., Liebman, M., Polley, H. W., Quijas, S., & Scherer-Lorenzen, M. (2017). Benefits of increasing plant diversity in sustainable agroecosystems. *Journal of Ecology*, *105*(4), 871–879. https://doi.org/10.1111/1365-2745.12789

Kefalas, G., Poirazidis, K., Xofis, P., & Kalogirou, S. (2018). Mapping and Understanding the Dynamics of Landscape Changes on Heterogeneous Mediterranean Islands with the Use of OBIA: The Case of Ionian Region, Greece. *Sustainability 2018, Vol. 10, Page 2986*, *10*(9), 2986. https://doi.org/10.3390/SU10092986

Loizzo, R.; Daraio, M.; Guarini, R.; Longo, F.; Lorusso, R.; Dini, L.; Lopinto, E. (2019). *PRISMA MISSION STATUS AND PERSPECTIVE*. https://ieeexplore.ieee.org/stamp/stamp.jsp?tp=&arnumber=8899272&tag=1

Madonsela, S., Cho, M. A., Ramoelo, A., & Mutanga, O. (2017a). Remote sensing of species diversity using Landsat 8 spectral variables. *ISPRS Journal of Photogrammetry and Remote Sensing*, *133*, 116–127. https://doi.org/10.1016/j.isprsjprs.2017.10.008

Madonsela, S., Cho, M. A., Ramoelo, A., & Mutanga, O. (2017b). Remote sensing of species diversity using Landsat 8 spectral variables. *ISPRS Journal of Photogrammetry and Remote Sensing*, *133*, 116–127. https://doi.org/10.1016/J.ISPRSJPRS.2017.10.008

Markham, K., Frazier, A. E., Singh, K. K., & Madden, M. (2023). A review of methods for scaling remotely sensed data for spatial pattern analysis. *Landscape Ecology*, *38*(3), 619–635. https://doi.org/10.1007/s10980-022-01449-1

Martinez, M. H. (2012). *UNIVERSIDAD POLITÉCNICA DE MADRID SENSING DATA USING TIME SERIES ANALYSIS : FORESTRY AND TESIS DOCTORAL MARGARITA HUESCA MARTÍNEZ Ingeniera de Montes MADRID , 2012 MADRID , 2012*.

Michela, P., Febbraro Mirko, D., Luisa, C., Jan, D., Milan, C., Petr, K., Maria Laura, C., Duccio, R., Michele, T., Vítězslav, M., Petra, Š., Dominika, P., Jana, M., Jan, W., & Marco, M. (2022). The relationship between spectral and plant diversity: disentangling the influence of metrics and habitat types. *In Review*, 1–22. https://doi.org/10.1101/2022.09.05.506583

Miraglio, T., Adeline, K., Huesca, M., Ustin, S., & Briottet, X. (2022). Assessing vegetation traits estimates accuracies from the future SBG and biodiversity hyperspectral missions over two Mediterranean Forests. *International Journal of Remote Sensing*, *43*(10), 3537–3562. https://doi.org/10.1080/01431161.2022.2093143

Müller, R., Bachmann, M., Chlebek, C., Krawczyk, H., de Miguel, A., Palubinskas, G., Schneider, M., Schwind, P., Storch, T., Mogulsky, V., & Sang, B. (2012). The EnMAP Hyperspectral Satellite Mission An Overview and Selected Concepts. *3th Annual Hyperspectral Imaging Conference (HSI 2012), Istituto Nazionale Di Geofisica e Vulcanologia (INGV), May 15-16, Rome, Italy*, *May*, 39–44. http://elib.dlr.de/78214/1/HSI2012.pdf

Net), C. Z. C. N. (CZ. (2020). *San Joaquin Experimental Range. Sierra Critical Zone Observatory*. https://czo-archive.criticalzone.org/sierra/infrastructure/field-area/flux-tower-at-san-joaquin-experimental-range/

Newman, T. F., & Duncan, D. a. (1973). *Vertebrate fauna of the San Joaquin Experimental Range, California: a checklist. General Te*, 17.

Ollinger, S. V. (2011). Sources of variability in canopy reflectance and the convergent properties of plants. *New Phytologist*, *189*(2), 375–394. https://doi.org/10.1111/j.1469-8137.2010.03536.x

Onyia, N. N., Balzter, H., & Berrio, J. C. (2019). Spectral Diversity Metrics for Detecting Oil Pollution Effects on Biodiversity in the Niger Delta. *Remote Sensing 2019, Vol. 11, Page 2662*, *11*(22), 2662. https://doi.org/10.3390/RS11222662

Palmer, M. W., Earls, P. G., Hoagland, B. W., White, P. S., & Wohlgemuth, T. (2002). Quantitative tools for perfecting species lists. *Environmetrics*, *13*(2), 121–137. https://doi.org/10.1002/env.516

Pereira, R., & Palmeirim, M. J. (2013). Latitudinal Diversity Gradients in New World Bats: Are They a Consequence of Niche Conservatism? *PLoS ONE*, *8*(7), 69245. https://doi.org/10.1371/journal.pone.0069245

Pervez, W., Uddin, V., Khan, S. A., & Khan, J. A. (2016). Satellite-based land use mapping: comparative analysis of Landsat-8, Advanced Land Imager, and big data Hyperion imagery. *Journal of Applied Remote Sensing*, *10*(2), 026004. https://doi.org/10.1117/1.jrs.10.026004

Plana, Eduard., Fons, Marc., Serra, Marta., Borràs, Mariona., Vilalta, O. (2016). Fire and Fore S T Fires in the Mediterranean ; a Relationship Story Between. *Efirecom. Efficient Fire Risk Communication for Resilient Societies*.

Purcell, K. L., Drynan, D. A., & Mazzocco, K. M. (2007). *Vertebrate Fauna of the San Joaquin Experimental Range , California : an annotated checklist based on 70 years of observations*.

Raft, A., & Oliier, H. (2011). Forest restoration, biodiversity and ecosystem functioning. *BMC Ecology*, 1–21.

Rast, M., & Painter, T. H. (2019). Earth Observation Imaging Spectroscopy for Terrestrial Systems: An Overview of Its History, Techniques, and Applications of Its Missions. *Surveys in Geophysics*, *40*(3), 303–331. https://doi.org/10.1007/s10712-019-09517-z

Rocchini, D., Hernández-Stefanoni, J. L., & He, K. S. (2015). Advancing species diversity estimate by remotely sensed proxies: A conceptual review. *Ecological Informatics*, *25*, 22–28. https://doi.org/10.1016/j.ecoinf.2014.10.006

Roger N. Clark, Gregg A. Swayze, Richard Wise, K. Eric Livo, Todd M. Hoefen, Raymond F. Kokaly, and S. J. S. (1993). *USGS Spectroscopy Lab - Spectral Library*. Mapping Minerals with Imaging Spectroscopy. http://speclab.cr.usgs.gov/spectral-lib.html

Roth, K. L., Roberts, D. A., Dennison, P. E., Alonzo, M., Peterson, S. H., & Beland, M. (2015). Differentiating plant species within and across diverse ecosystems with imaging spectroscopy. *Remote Sensing of Environment*, *167*, 135–151. https://doi.org/10.1016/j.rse.2015.05.007

Silveira, E. M. O., Radeloff, V. C., Martinuzzi, S., Martínez Pastur, G. J., Rivera, L. O., Politi, N., Lizarraga, L., Farwell, L. S., Elsen, P. R., & Pidgeon, A. M. (2021). Spatio-temporal remotely sensed indices identify hotspots of biodiversity conservation concern. In *Remote Sensing of Environment* (Vol. 258). https://doi.org/10.1016/j.rse.2021.112368

Singh, A. (1993). Principal components analysis in remote sensing. *International Geoscience and Remote Sensing Symposium (IGARSS)*, *4*, 1680–1682. https://doi.org/10.1109/IGARSS.1993.322441

Singh, D., & Singh, B. (2022). Feature wise normalization: An effective way of normalizing data. *Pattern Recognition*, *122*, 108307. https://doi.org/10.1016/j.patcog.2021.108307

Sousa, D., & Small, C. (2018). Multisensor analysis of spectral dimensionality and soil diversity in the great central valley of California. *Sensors (Switzerland)*, *18*(2). https://doi.org/10.3390/s18020583

Stahle, D. W., Griffin, R. D., Meko, D. M., Therrell, M. D., Edmondson, J. R., Cleaveland, M. K., Stahle, L. N., Burnette, D. J., Abatzoglou, J. T., Redmond, K. T., Dettinger, M. D., & Cayan, D. R. (2013). The Ancient Blue Oak Woodlands of California: Longevity and Hydroclimatic History. *Earth Interactions*, *17*(12), 1–23. https://doi.org/10.1175/2013EI000518.1

T. Cocks, R. Jenssen, A. Stewart, I. W. and T. S. (1998). The HyMap. *October*, 1–6. http://www.hyvista.com/wp_11/wp-content/uploads/2011/02/EARSEL98_HyMap.pdf

Thompson, D. R., Gao, B. C., Green, R. O., Roberts, D. A., Dennison, P. E., & Lundeen, S. R. (2015). Atmospheric correction for global mapping spectroscopy: ATREM advances for the HyspIRI preparatory campaign. *Remote Sensing of Environment*, *167*, 64–77. https://doi.org/10.1016/j.rse.2015.02.010

Ullrich, P. A., Xu, Z., Rhoades, A. M., Dettinger, M. D., Mount, J. F., Jones, A. D., & Vahmani, P. (2018). California's Drought of the Future: A Midcentury Recreation of the Exceptional Conditions of 2012–2017. *Earth's Future*, *6*(11), 1568–1587. https://doi.org/10.1029/2018EF001007

UNEP. (2021). Making Peace with Nature. *Making Peace with Nature*. https://doi.org/10.18356/9789280738377

United Nation Environment Programme-UNEP (UNEP). (2018). *CBD Press Brief. Biodiversity and the Sustainable Development Goals*. https://www.cbd.int/cop/cop-14/media/briefs/en/cop14-press-brief-sdgs.pdf

(United nations Department of Economic and Social Affairs), D. (2021). *Reducing poverty and inequality in rural areas: key to inclusive development | DISD*. https://www.un.org/development/desa/dspd/2021/05/reducing-poverty/

Viedma, O., Torres, I., Pérez, B., & Moreno, J. M. (2012). Modeling plant species richness using reflectance and texture data derived from QuickBird in a recently burned area of Central Spain. *Remote Sensing of Environment*, *119*, 208–221. https://doi.org/10.1016/J.RSE.2011.12.024

Whittaker, R. H. (1972). Evolution and Measurement of Species Diversity Published by : Wiley Stable URL : https://www.jstor.org/stable/1218190 REFERENCES Linked references are available on JSTOR for this article : You may need to log in to JSTOR to access the linked references . *Ethics*, *21*(2), 213–251.

WHO (World Health Organisation). (2015). *Biodiversity and Health*. https://www.who.int/news-room/fact-sheets/detail/biodiversity-and-health

Zhang, L., Zhang, Z., Luo, Y., Cao, J., Xie, R., & Li, S. (2021). Integrating satellite-derived climatic and

vegetation indices to predict smallholder maize yield using deep learning. *Agricultural and Forest Meteorology*, *311*. https://doi.org/10.1016/J.AGRFORMET.2021.108666

Zhao, W., Qu, Y., Zhang, L., & Li, K. (2022). Spatial-aware SAR-optical time-series deep integration for crop phenology tracking. *Remote Sensing of Environment*, *276*(December 2021), 113046. https://doi.org/10.1016/j.rse.2022.113046

Zhu, Z. (2017). Change detection using landsat time series: A review of frequencies, preprocessing, algorithms, and applications. *ISPRS Journal of Photogrammetry and Remote Sensing*, *130*(July 2017), 370–384. https://doi.org/10.1016/j.isprsjprs.2017.06.013

7. APPENDIX

7.1. Spectral Curves of Clusters

The average spectral reflectance was derived from the mean reflectance curves of pixels belonging to each cluster in the considered images. Spectral profiles demonstrate significant variation among species across the spectra and overall albedo. Figure 21 to Figure 26 below shows the spectral curves of clusters in AVIRIS-NG, spectrally upscaled 4m image, spatially upscaled 16m image, spatially upscaled 30m image, simulated Landsat and Landsat 8 data.

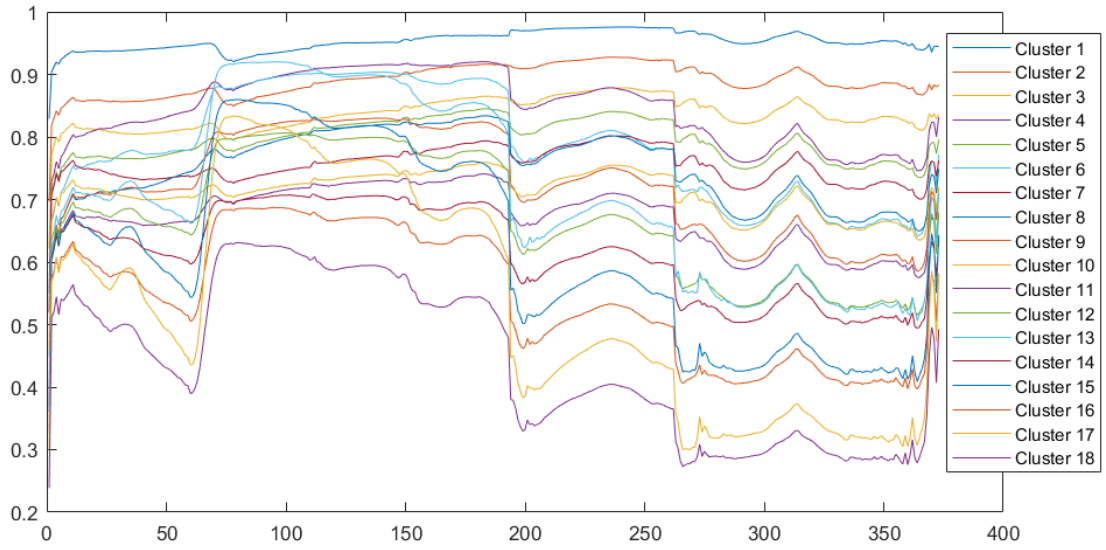

Figure 21 Average Spectral Reflectance of Clusters identified in AVIRIS-NG.

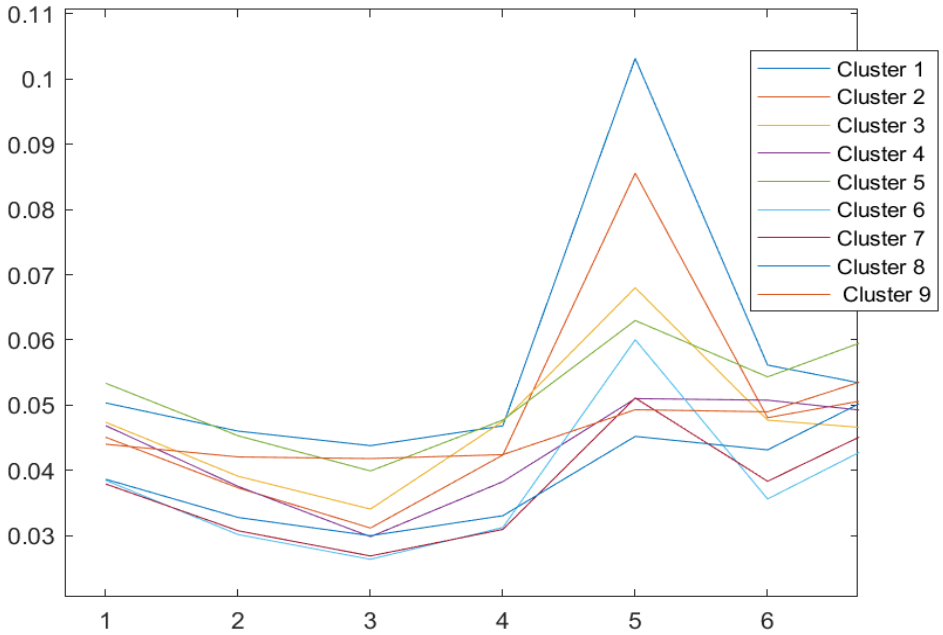

Figure 22 Average Spectral Reflectance of Clusters identified in Spectrally Upscaled 4m image (7 bands)

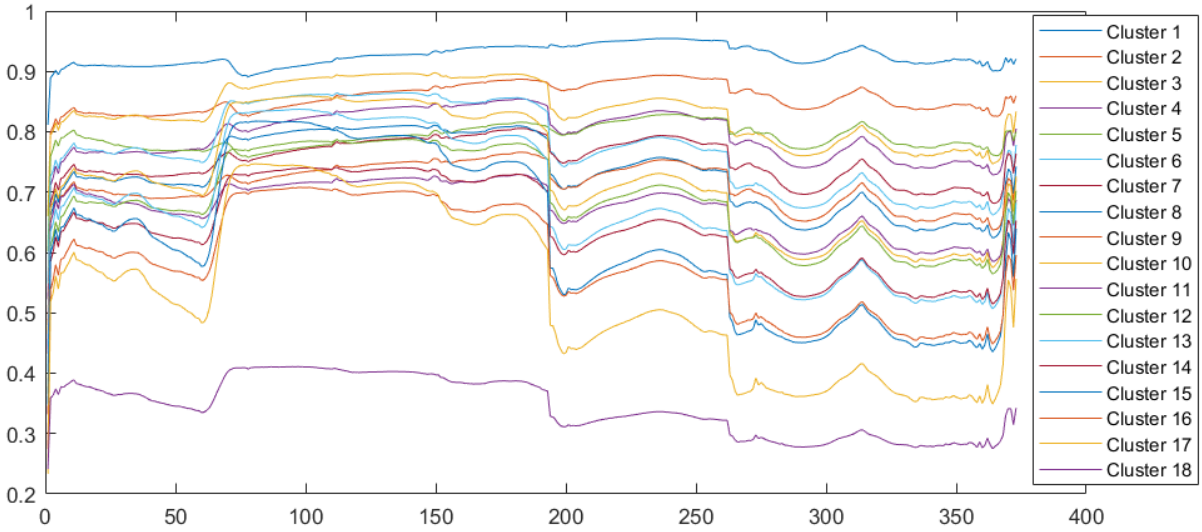

Figure 23 Average Spectral Reflectance of Clusters identified in the Spatially Upscaled 16m image.

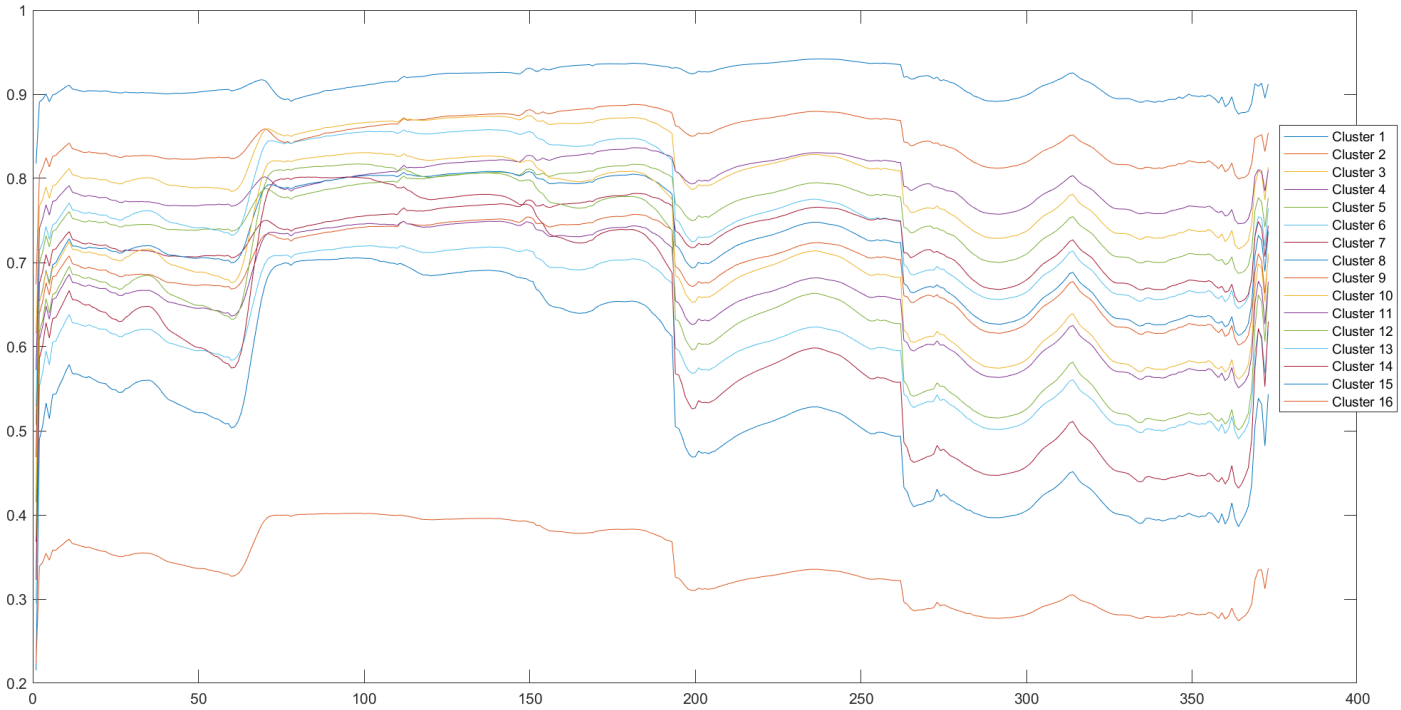

Figure 24 Average Spectral Reflectance of Clusters identified in the Spatially Upscaled 30 image.

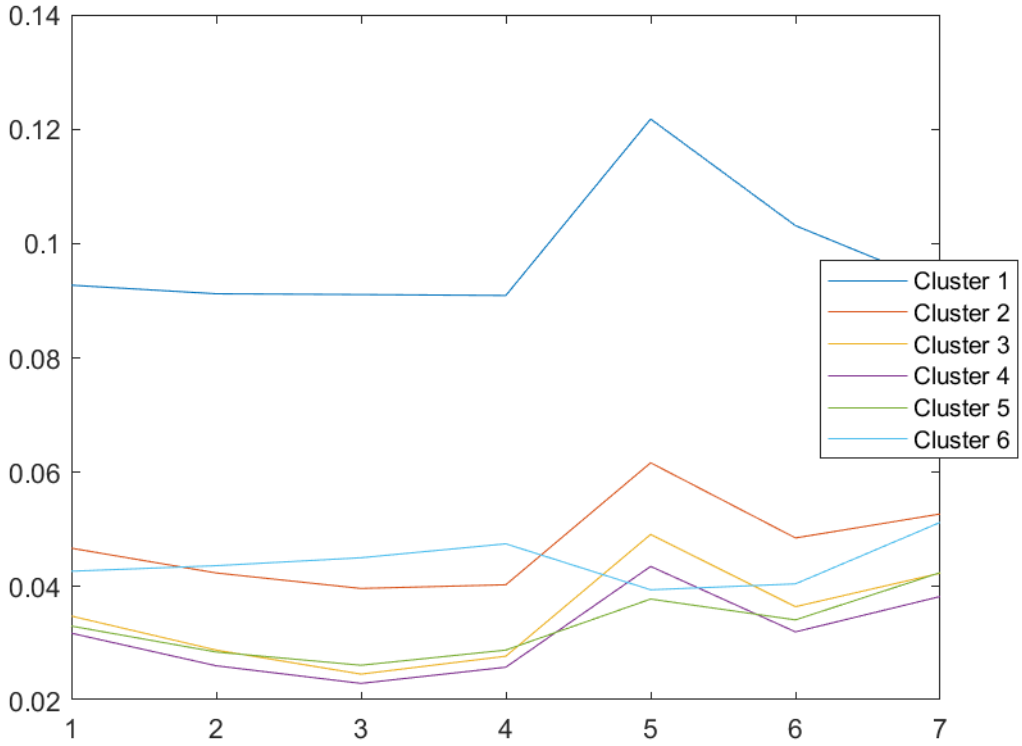

Figure 25 Average Spectral Reflectance of Clusters identified in Simulated Landsat.

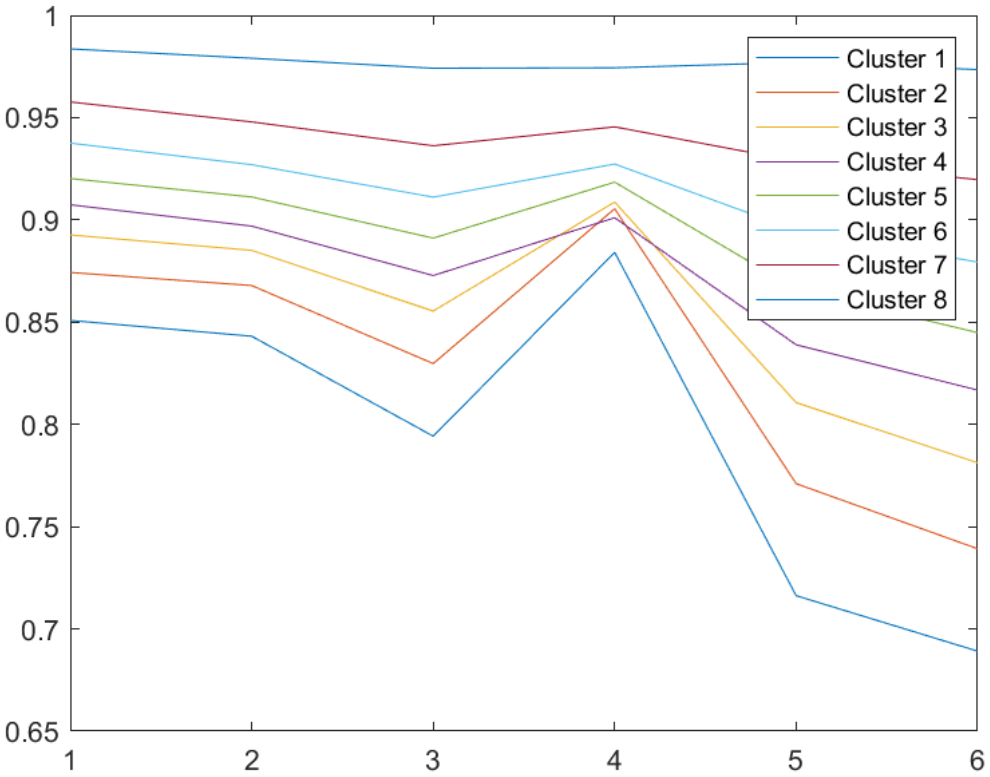

Figure 26 Average Spectral Reflectance of Clusters identified in Landsat 8

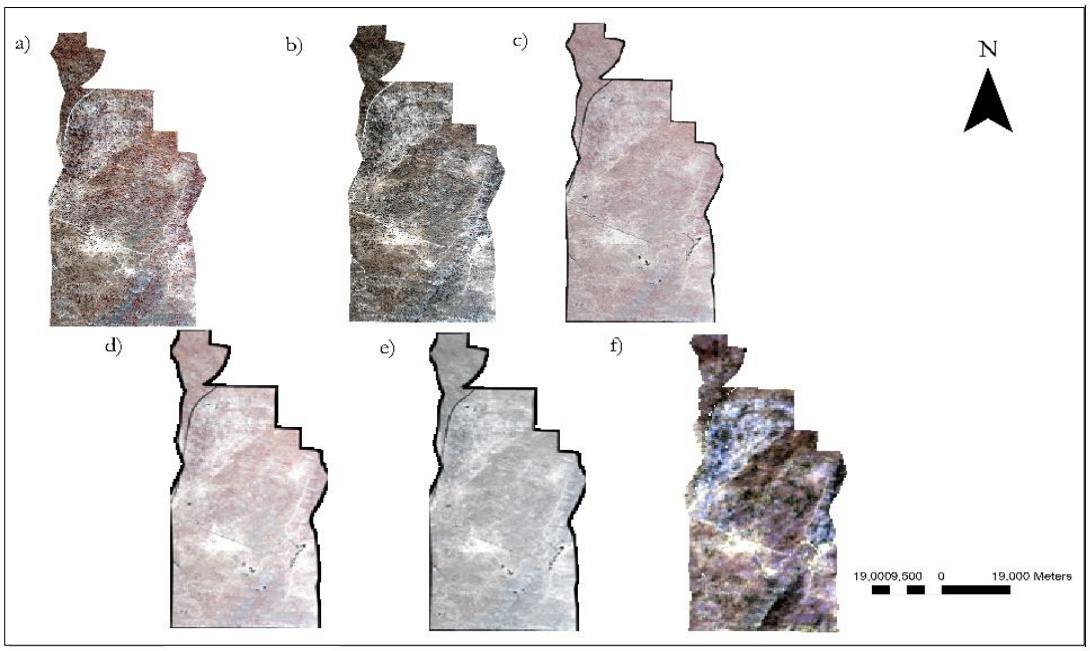

Figure 27 RGB images for a) AVIRIS-NG (4m) b) Spectrally Upscaled 4m image (7 bands) c) Spatially Upscaled 16m image (373 bands) d) Spatially upscaled 30m image (373 bands) e)Simulated Landsat (30m with 7 bands) and f) Landsat 8 data (30m with 7 bands).

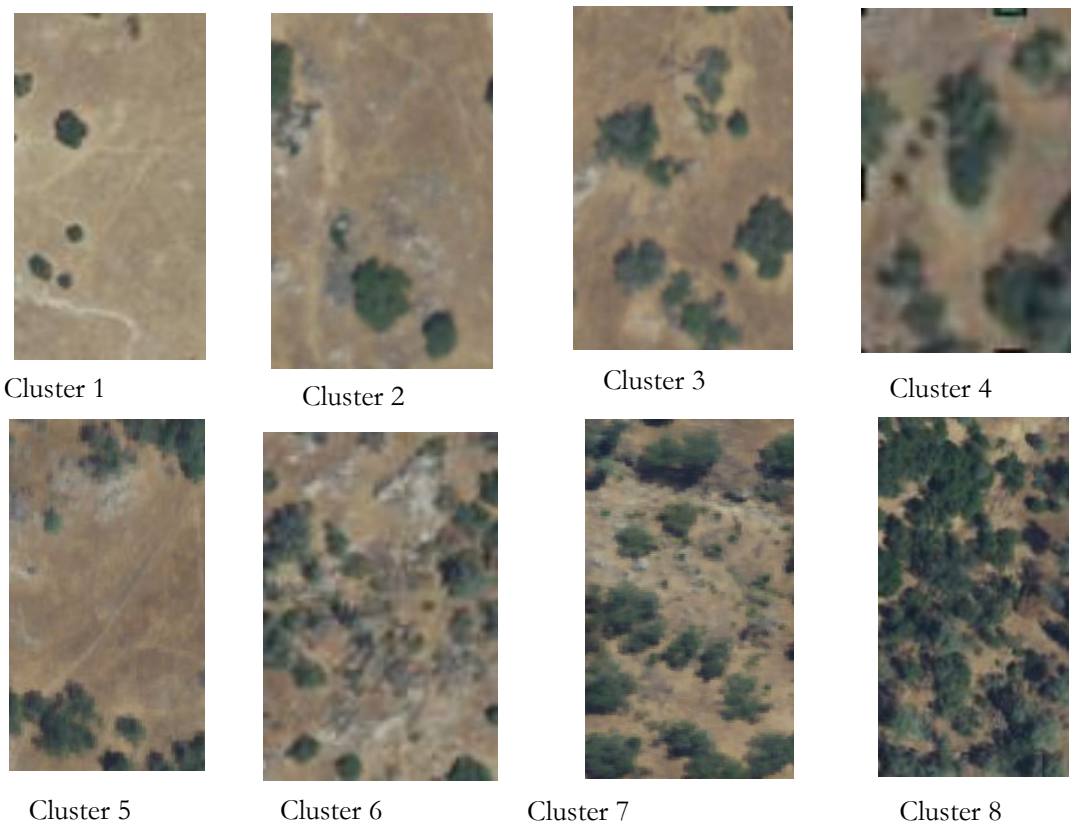

Figure 28 Examples of zoom-in areas of clusters derived in Landsat 8 data

Table 5 Eigenvectors of PCA Analysis in Simulated Landsat

Eigenvector	Band 1	Band 2	Band 3	Band 4	Band 5	Band 6	Band 7
Eig. 1	0.35	0.36	0.36	0.39	0.24	0.43	0.48
Eig. 2	-0.23	-0.19	-0.19	0.01	-0.70	0.28	0.55
Eig. 3	0.51	0.39	0.19	-0.03	-0.57	-0.47	-0.08
Eig. 4	0.36	0.05	-0.25	-0.78	0.23	0.04	0.38
Eig. 5	0.33	0.07	-0.27	-0.05	-0.21	0.68	-0.55
Eig. 6	-0.41	0.25	0.67	-0.48	-0.14	0.25	-0.14
Eig. 7	-0.40	0.78	-0.47	0.04	0.06	-0.04	0.03

Table 6 Eigenvectors of PCA Analysis in Landsat 8

Eigenvector	Band 1	Band 2	Band 3	Band 4	Band 5	Band 6	Band 7
Eig. 1	0.27	0.28	0.27	0.16	0.36	0.53	0.59
Eig. 2	0.23	-0.08	-0.07	0.09	-0.92	0.14	0.24
Eig. 3	-0.63	-0.20	-0.21	0.04	-0.49	0.48	0.21
Eig. 4	-0.34	0.00	0.43	0.72	-0.19	-0.35	-0.11
Eig. 5	0.22	0.13	-0.22	0.34	-0.17	0.52	-0.69
Eig. 6	0.11	0.01	-0.78	0.45	0.14	-0.29	0.26
Eig. 7	-0.55	0.80	-0.17	-0.14	0.00	0.05	-0.01

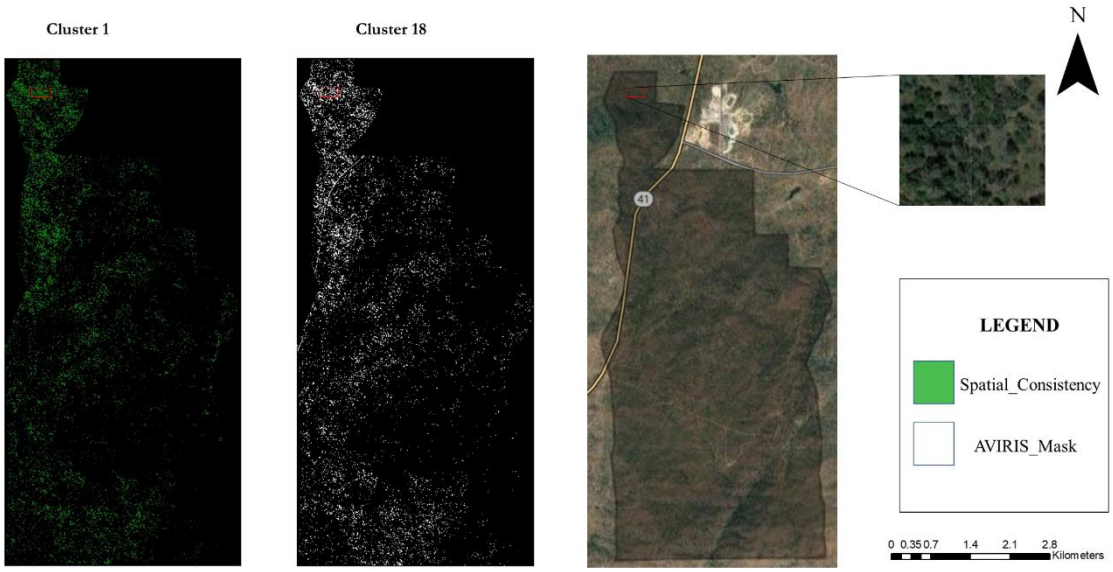

Figure 29 Spatially Consistent Clusters In Spectrally Upscaled 4m Image And AVIRIS-NG Together with a Corresponding Region In High Resolution.

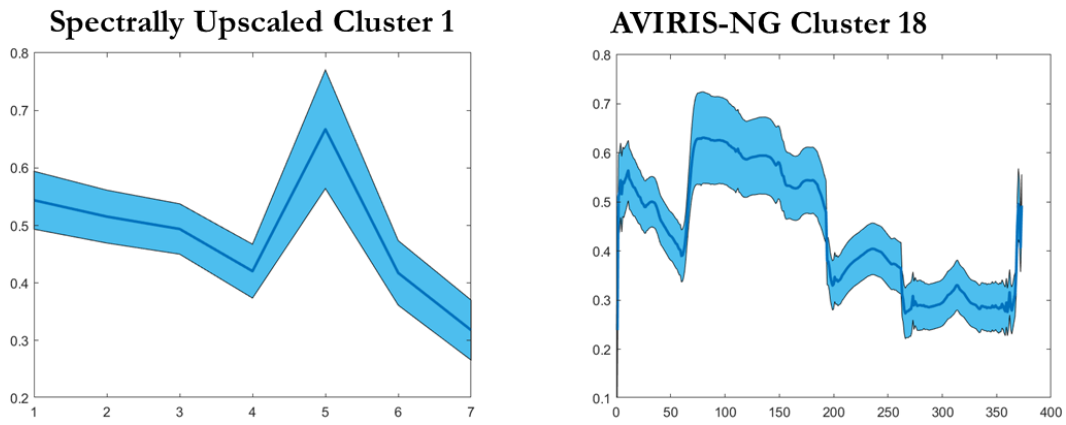

Figure 30 Corresponding Spectral Profiles of Spectral Upscaled 4m image Cluster 1 and AVIRIS-NG Cluster 18.

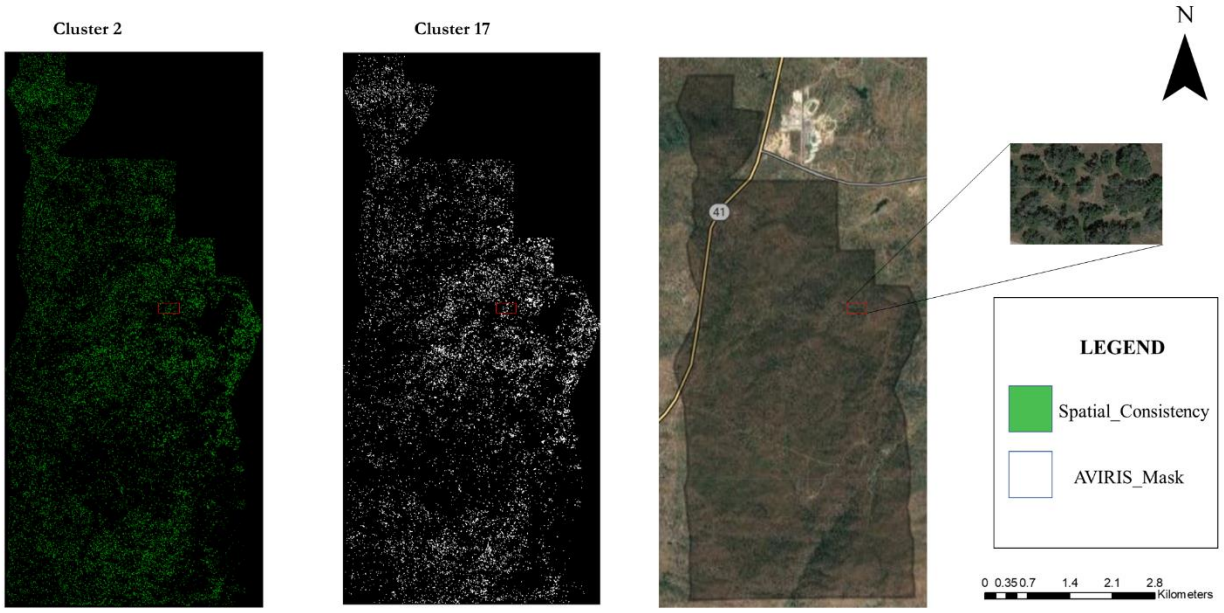

Figure 31 Spatially Consistent Clusters In Spectrally Upscaled 4m Image And AVIRIS-NG Together with a Corresponding Region In High Resolution.

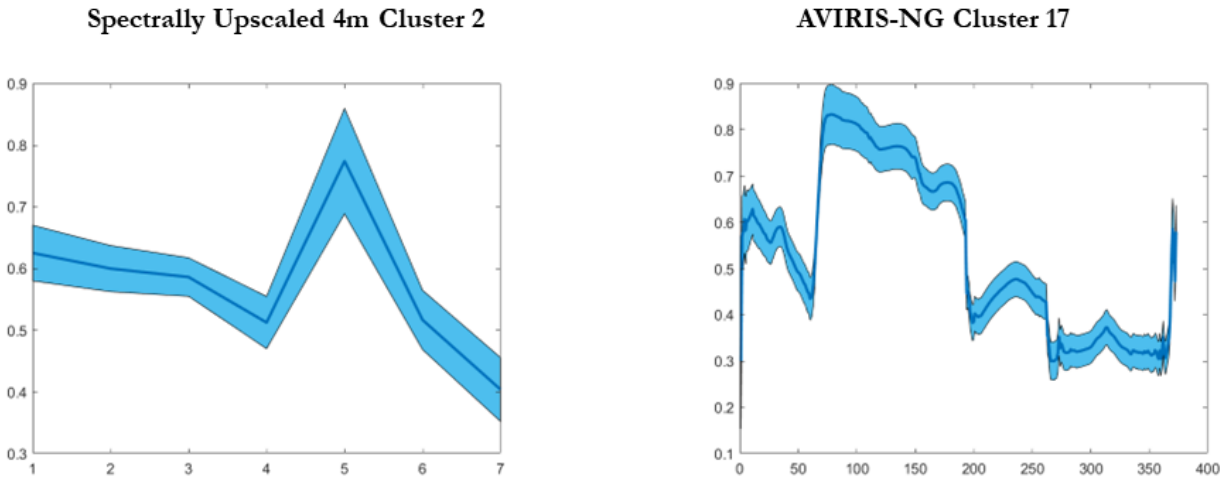

Figure 32 Corresponding Spectral Profiles of Spectral Upscaled 4m image Cluster 2 and AVIRIS-NG Cluster 17.

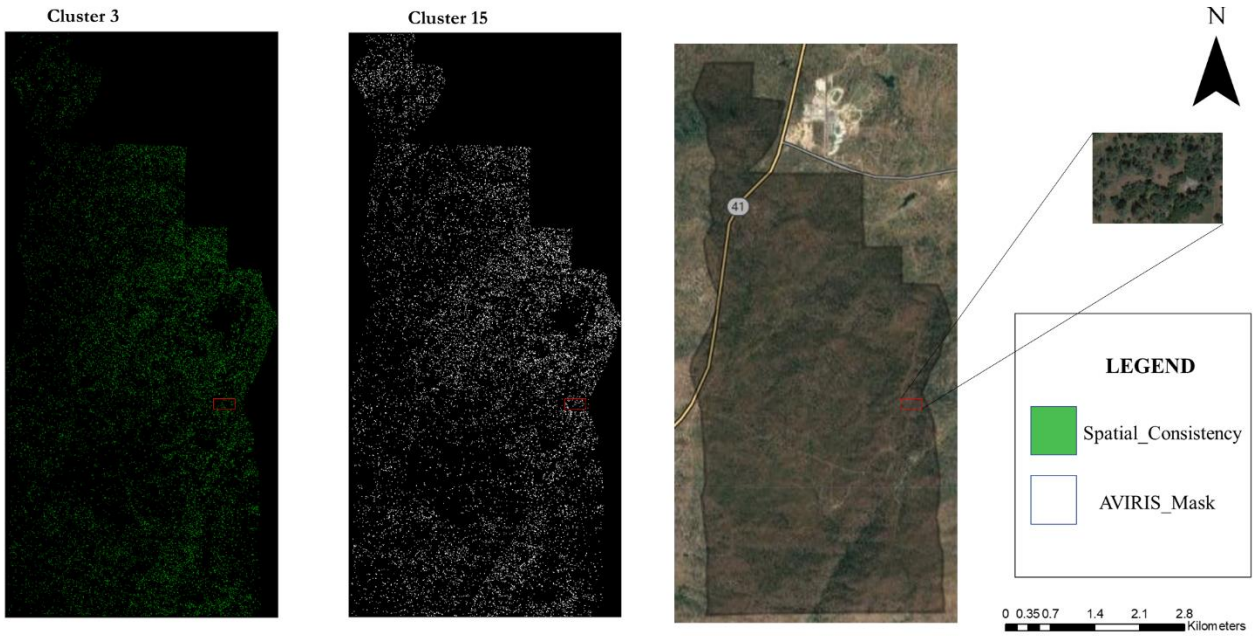

Figure 33 Spatially Consistent Clusters In Spectrally Upscaled 4m Image And AVIRIS-NG Together with a Corresponding Region In High Resolution.

.

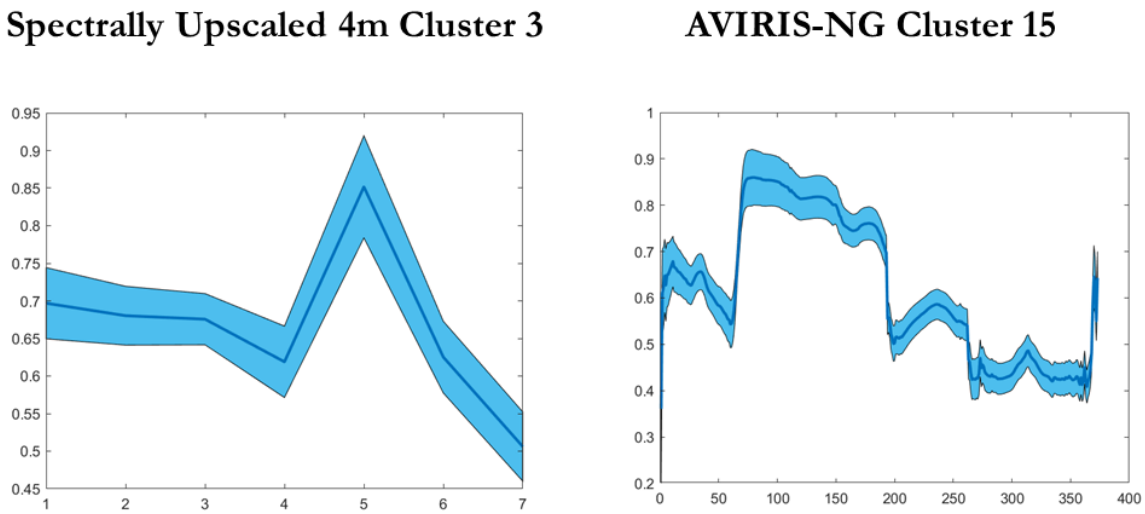

Figure 34 Corresponding Spectral Profiles of Spectral Upscaled 4m image Cluster 3 and AVIRIS-NG Cluster 15.

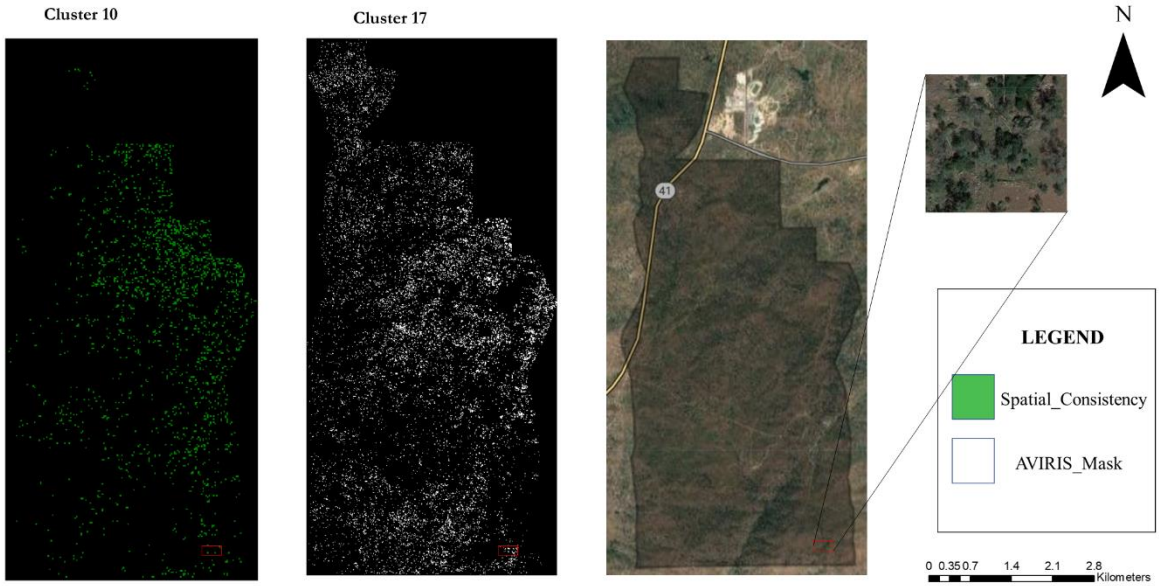

Figure 36 Spatially Consistent Clusters In Spatially Upscaled 16m Image And AVIRIS-NG together with a Corresponding Region In High Resolution.

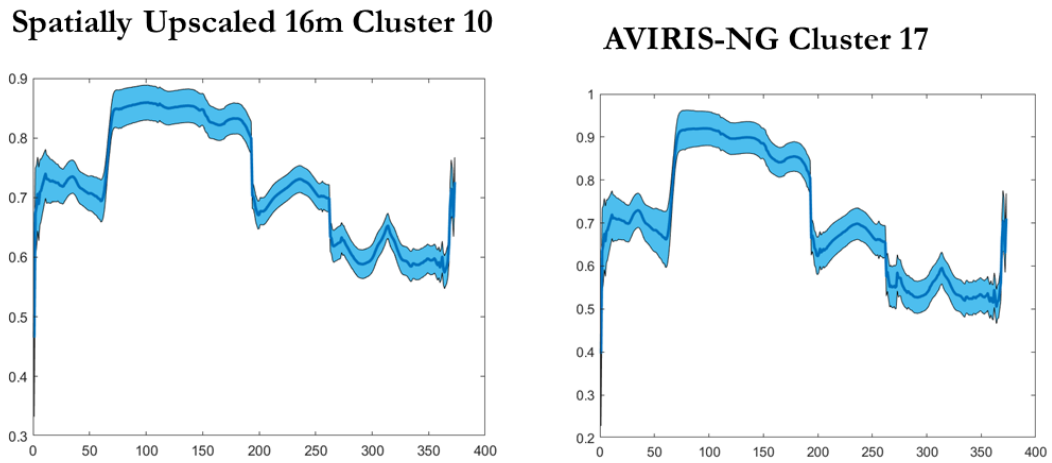

Figure 35 Corresponding Spectral Profiles of Spatially Upscaled 16m image Cluster 10 and AVIRIS-NG Cluster 17.

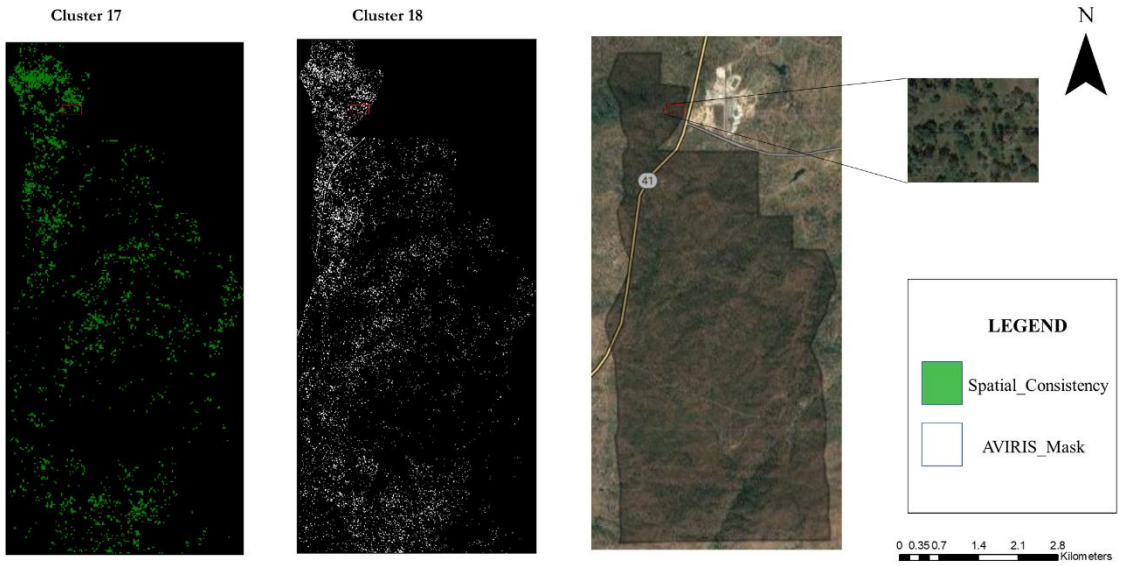

Figure 37 Spatially Consistent Clusters In Spatially Upscaled 16m Image And AVIRIS-NG Together with a Corresponding Region In High Resolution.

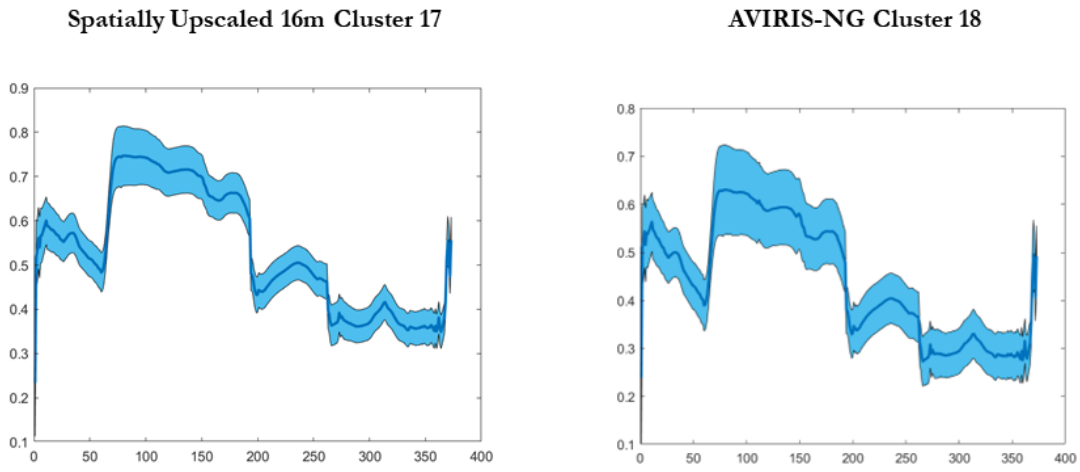

Figure 38 Corresponding Spectral Profiles of Spatially Upscaled 16m image Cluster 17 and AVIRIS-NG Cluster 18.

Figure 40 Spatially Consistent Clusters in Spatially Upscaled 16m Image And AVIRIS-NG together with a Corresponding Region In High Resolution.

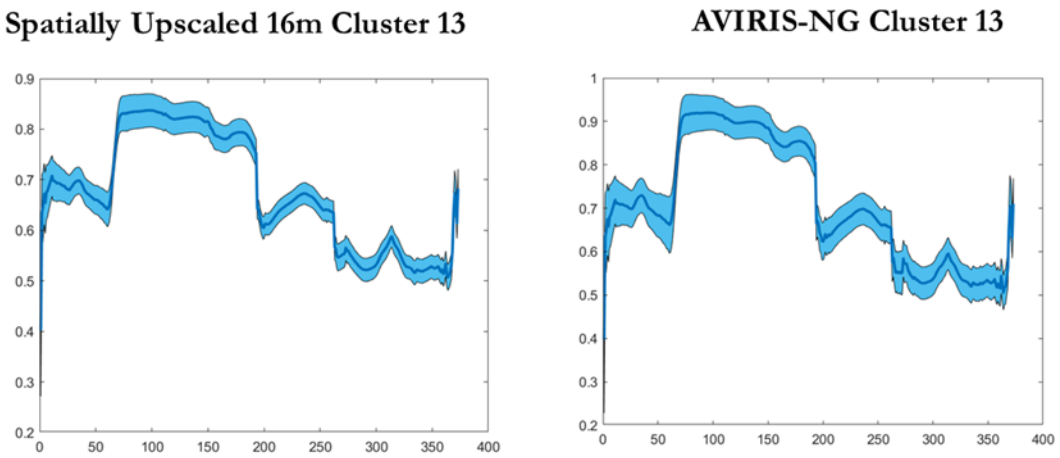

Figure 39 Corresponding Spectral Profiles of Spatially Upscaled 16m image Cluster 13 and AVIRIS-NG Cluster 13.

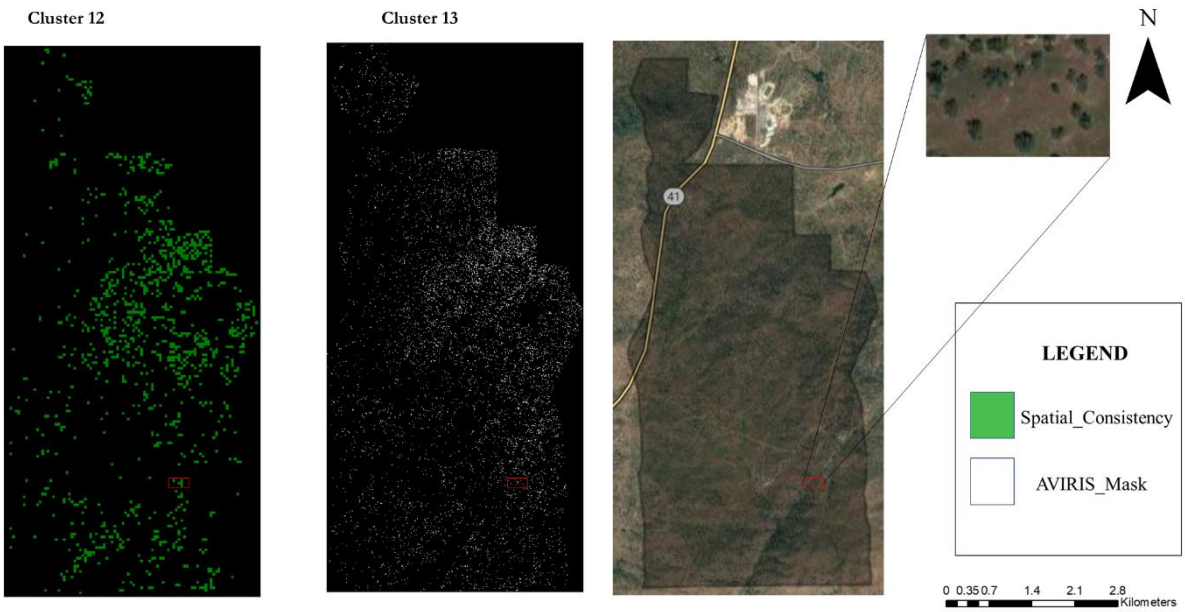

Figure 41 Corresponding Spectral Profiles of Spatially Upscaled 16m image Cluster 13 and AVIRIS-NG Cluster 13.

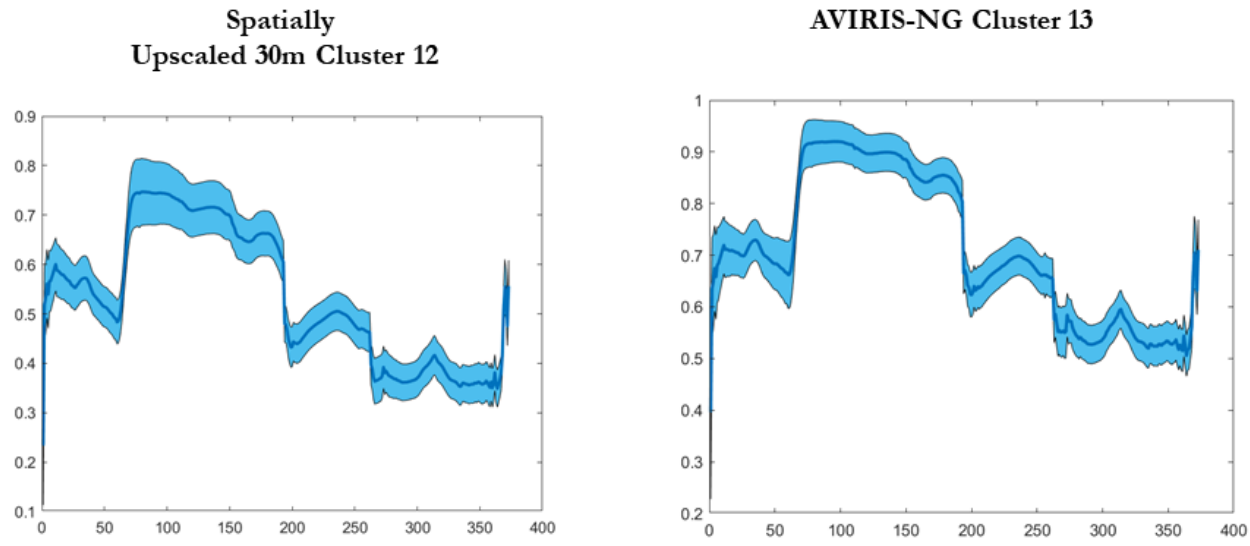

Figure 42 Corresponding Spectral Profiles of Spatially Upscaled 16m image Cluster 12 and AVIRIS-NG Cluster 13.

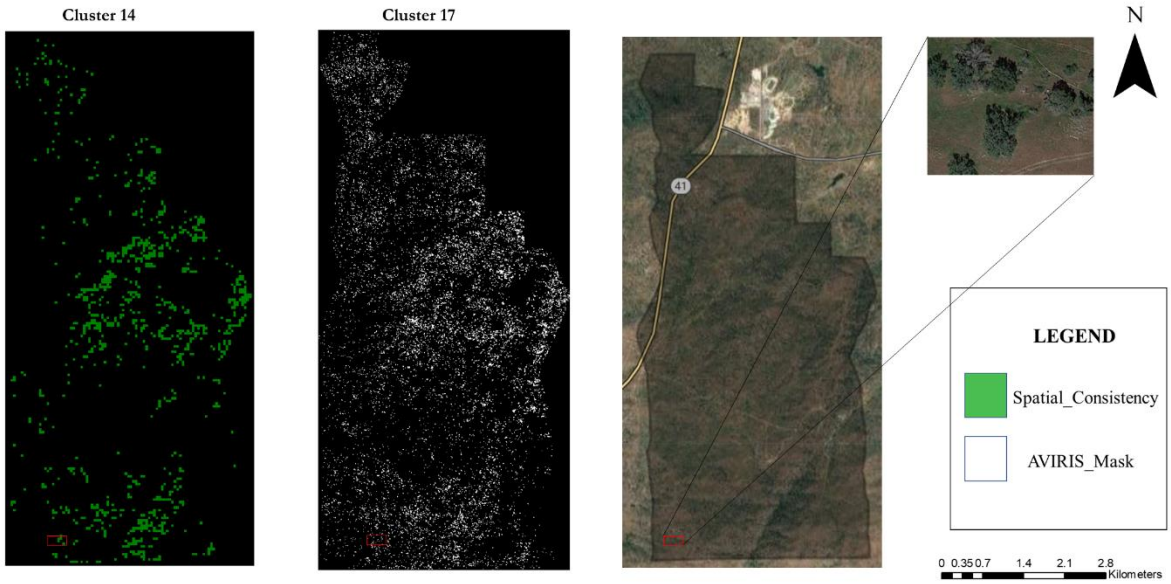

Figure 43 Spatially Consistent Clusters In Spatially Upscaled 30m Image And AVIRIS-NG Together with a Corresponding Region In High Resolution.

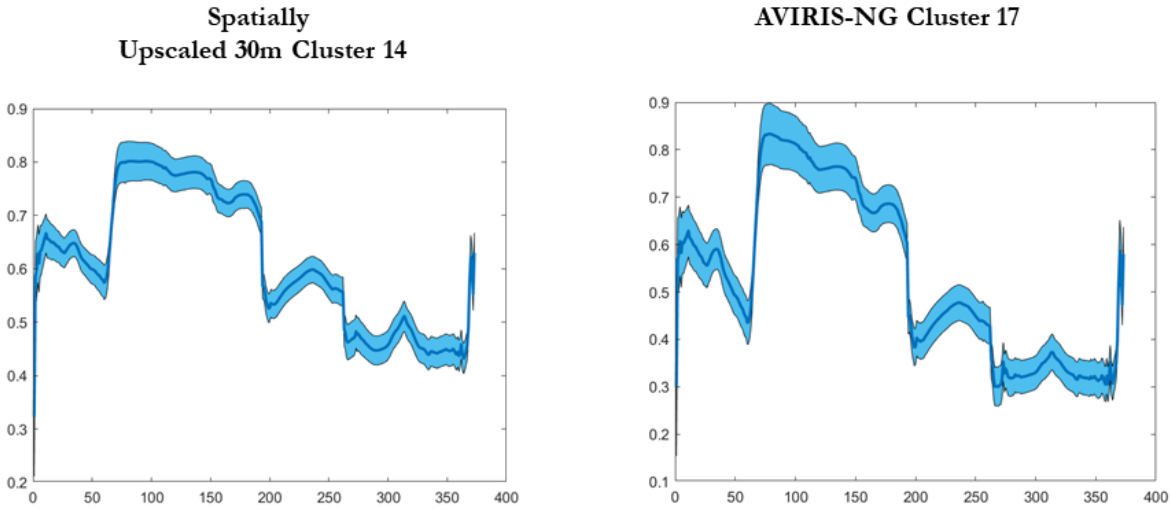

Figure 44 Corresponding Spectral Profiles of Spatially Upscaled 16m image Cluster 14 and AVIRIS-NG Cluster 17.

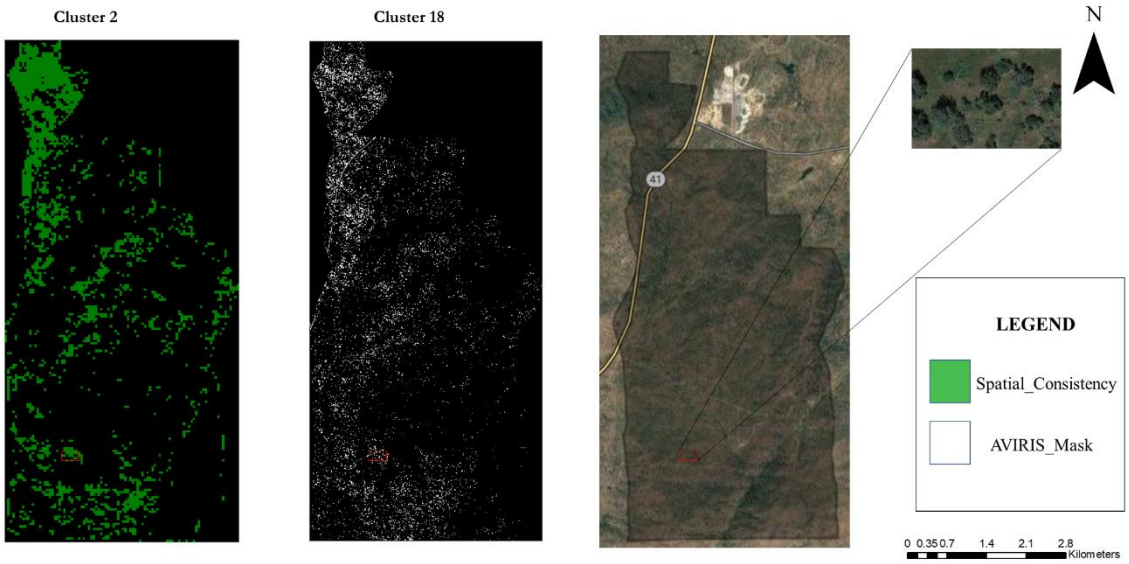

Figure 47 Spatially Consistent Clusters In Simulated Landsat Image And AVIRIS-NG Together with a Corresponding Region In High Resolution.

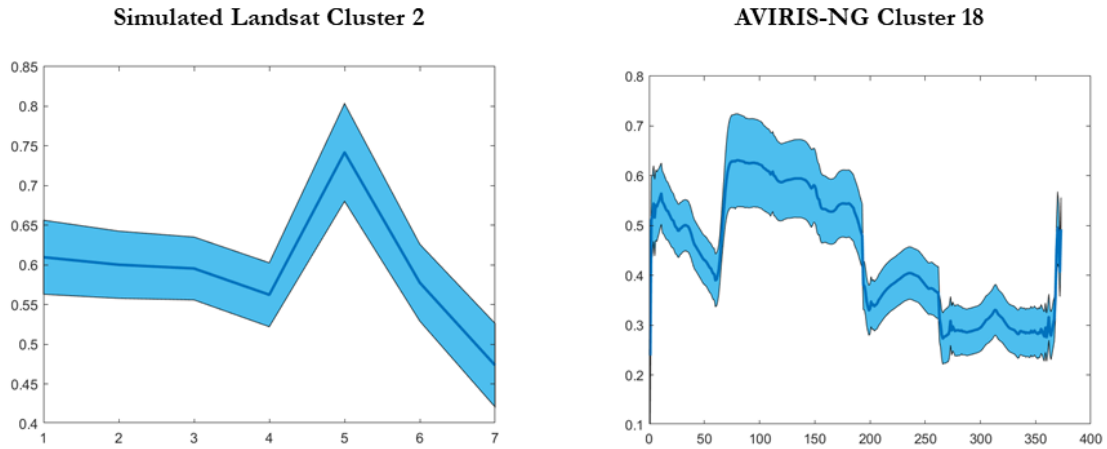

Figure 45 Corresponding Spectral Profiles of Simulated Landsat Cluster 2 and AVIRIS-NG Cluster 18.

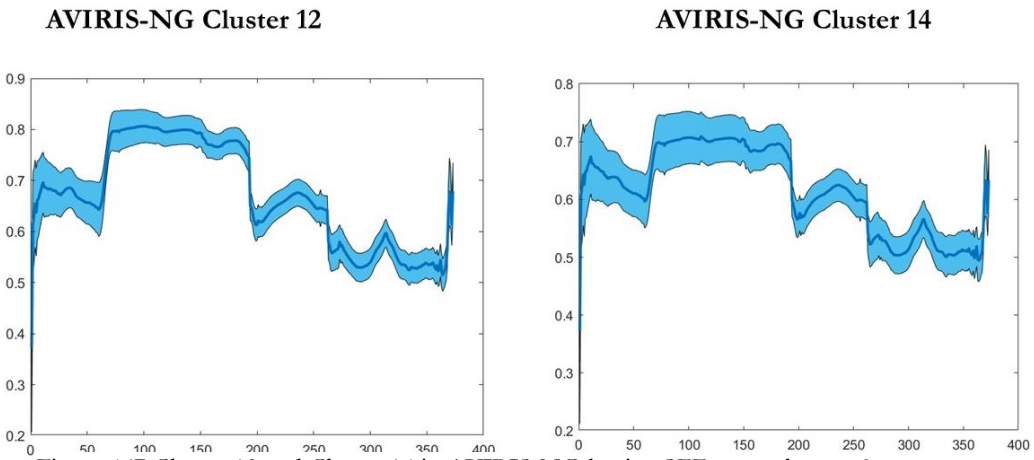

Figure 467 Cluster 12 and Cluster 14 in AVIRIS-NG having SFF score close to 0